Microwave Sounder Cloud Detection Using a Collocated High-Resolution Imager and Its Impact on Radiance Assimilation in Tropical Cyclone Forecasts

HYOJIN HAN,[a,b] JUN LI,[a] MITCH GOLDBERG,[c] PEI WANG,[a,d] JINLONG LI,[a] ZHENGLONG LI,[a] B.-J. SOHN,[e] AND JUAN LI[f]

[a] *Cooperative Institute for Mesoscale Meteorological Studies, University of Wisconsin–Madison, Madison, Wisconsin*
[b] *National Institute of Meteorological Sciences, Korea Meteorological Administration, Jeju-do, South Korea*
[c] *NOAA/NESDIS, Joint Polar Satellite System, Lanham, Maryland*
[d] *Department of Atmospheric and Oceanic Sciences, University of Wisconsin–Madison, Madison, Wisconsin*
[e] *School of Earth and Environmental Science, Seoul National University, Seoul, South Korea*
[f] *Numerical Weather Prediction Center, China Meteorological Administration, Beijing, China*

(Manuscript received 25 August 2015, in final form 15 July 2016)

ABSTRACT

Accurate cloud detection is one of the most important factors in satellite data assimilation due to the uncertainties associated with cloud properties and their impacts on satellite-simulated radiances. To enhance the accuracy of cloud detection and improve radiance assimilation for tropical cyclone (TC) forecasts, measurements from the Advanced Microwave Sounding Unit-A (AMSU-A) on board the *Aqua* satellite and the Advanced Technology Microwave Sounder (ATMS) are collocated with high spatial resolution cloud products from the Moderate Resolution Imaging Spectroradiometer (MODIS) on board *Aqua* and the Visible Infrared Imager Radiometer Suite (VIIRS) on board the *Suomi-National Polar-Orbiting Partnership* (*Suomi-NPP*) satellite. The cloud-screened microwave radiance measurements are assimilated for Hurricane Sandy (2012) and Typhoon Haiyan (2013) forecasts using the Weather Research and Forecasting (WRF) Model and the three-dimensional variational (3DVAR)-based Gridpoint Statistical Interpolation (GSI) data assimilation system. Experiments are carried out to determine the optimal thresholds of cloud fraction (CF) for minimizing track and intensity forecast errors. The results indicate that the use of high spatial resolution cloud products can improve the accuracy of TC forecasts by better eliminating cloud-contaminated microwave sounder field-of-views (FOVs). In conclusion, the combination of advanced microwave sounders and collocated high spatial resolution imagers is able to improve the radiance assimilation and TC forecasts. The methodology used in this study can be applied to process data from other pairs of microwave sounders and imagers on board the same platform.

1. Introduction

Advanced microwave and infrared (IR) sounders from polar-orbiting satellites have been widely used in global and regional numerical weather prediction (NWP) models, providing a positive impact on weather forecasts (McNally et al. 2000; Zapotocny et al. 2008; Tomaso and Bormann 2012; Joo et al. 2013). Unlike IR sounders, microwave sounders can penetrate more clouds and provide atmospheric thermodynamic information with a larger spatial coverage for radiance assimilation in NWP models; they are important measurement sources for improving weather forecasts. However, microwave sounders cannot penetrate precipitating and ice clouds, which need to be screened before use as input. It is, therefore, important to accurately detect if the microwave radiance is affected by clouds or not. Such cloud detection will reduce the cloud contamination from these kinds of observations in the data assimilation process.

The direct assimilation of cloudy radiances is still challenging due to the larger uncertainties in both NWP and radiative transfer models, and higher nonlinearity in cloudy regions for radiance assimilation (Bauer et al. 2011). Some progress has been made to assimilate microwave sounder radiances in cloudy skies at major

Corresponding author address: Hyojin Han, Cooperative Institute for Mesoscale Meteorological Studies, University of Wisconsin–Madison, 1225 West Dayton St., Madison, WI 53706.
E-mail: hyojin.han@ssec.wisc.edu

DOI: 10.1175/MWR-D-15-0300.1

operational centers, mainly using the Microwave Humidity Sounder (MHS) and Special Sensor Microwave Imager/Sounder (SSMIS) (Bauer et al. 2010; Geer et al. 2010; English 2014). To improve the microwave sounder radiance assimilation in both clear and cloudy skies, accurate cloud detection is still very important. The current approaches for cloud detection in microwave sounder radiance assimilation are mainly based on a comparison between the observed and the simulated microwave brightness temperatures (T_Bs) from background status (Bormann et al. 2013; Hu et al. 2014). For example, the Gridpoint Statistical Interpolation (GSI), the data assimilation system developed at the National Centers for Environmental Prediction (NCEP), uses quality control (QC) functions to screen cloud-affected microwave radiances. The QC functions apply a scattering index (SI) and a cloud liquid water path estimated with observed radiances and simulated T_Bs from the model background status (Hu et al. 2014). In the European Centre for Medium-Range Weather Forecasts (ECMWF) system, the QC for microwave sounders employs a first-guess departure in the window channel and an observation-based estimate of a liquid water path (Bormann et al. 2013). However, the current QC algorithms are not sufficiently accurate for some clouds, including precipitating and ice clouds, and the misclassification of clear (or cloudy) field-of-views (FOVs) results in a degraded performance of the data assimilation (Hu and Xue, 2007; Zou et al. 2013; Wang et al. 2014; Wang et al. 2015).

These difficulties stem from the coarser spatial resolution of microwave sounders [e.g., 48 km for Advanced Microwave Sounding Unit-A (AMSU-A) at nadir] (Diak et al. 1992; Weng et al. 2003). Cloud contamination is common within a microwave sounder FOV, and cloud detection with the current approaches might not be accurate enough for the radiance assimilation. An alternative cloud-detection method using subpixel cloud information has been developed; this subpixel cloud detection uses a collocated high spatial resolution cloud product from an imager on board the same platform as the microwave sounder, for example, the Moderate Resolution Imaging Spectroradiometer (MODIS) for the AMSU-A on board the *Aqua* satellite, and the Visible Infrared Imager Radiometer Suite (VIIRS) for the Advanced Technology Microwave Sounder (ATMS) on board the Joint Polar Satellite System (JPSS) *Suomi-National Polar-Orbiting Partnership* (*Suomi-NPP*) satellite. The advantage of this technique is that imagers such as MODIS and VIIRS can depict detailed cloud properties, such as cloud mask (CM), cloud-top pressure, cloud phase, etc., within a microwave footprint or FOV with very little error from temporal and geometric differences between the two instruments because the instruments observe the same target simultaneously. There have been efforts to develop the sounder subpixel cloud-detection methodology (Li et al. 2004) and to apply it for improving the assimilation of Atmospheric Infrared Sounder (AIRS) radiances (Wang et al. 2014, 2015). However, microwave sounder subpixel cloud detection is quite different from advanced IR sounder subpixel cloud detection. The IR sounders, such as MODIS and AIRS, usually see the same cloud properties. It is straightforward to use the MODIS CM for AIRS subpixel cloud detection, and to use the VIIRS CM for the Cross-track Infrared Sounder (CrIS) subpixel cloud detection. For a microwave sounder, such as AMSU-A and ATMS, it sees clouds differently than MODIS and VIIRS, respectively. Li and Zou (2013) detected cloud-contaminated microwave radiances using a similar approach, but the authors did not give clear evidence of improvement in forecast accuracy. Studies are needed on how to optimally use high spatial resolution imager cloud products for microwave sounder subpixel cloud detection, and furthermore, the impact on forecast accuracy.

Tropical cyclones (TCs) accompanied by heavy rainfall and strong winds are high impact weather systems, often causing damage to property and even fatalities when making landfall. Better prediction of TCs can reduce the social and economic damages; there is growing interest in enhanced satellite data assimilation to improve TC forecasts. Moreover, an assimilation study for TC forecasts is more easily accessible than for other larger atmospheric phenomena with limited computational resources because TCs can be simulated by a regional NWP model. Since microwave radiances may penetrate through nonprecipitating clouds, numerous studies have shown the capabilities of microwave radiances in data assimilation for TC forecasts (Goerss 2009; Liu et al. 2012; Schwartz et al. 2012; Zhang et al. 2013). Nevertheless, when ice and precipitation are present, they are opaque in the microwave wavelengths and have a complicated optical effect on remotely sensed radiances. Cloud-contaminated radiances potentially induce a negative impact on the analysis fields and subsequent TC forecasts since both the radiative transfer model and NWP model have relatively large uncertainties when precipitating clouds are present. The subpixel cloud detection was applied to eliminate the cloud-contaminated radiances that can introduce errors in the assimilation process. Moreover, by screening the cloud-contaminated satellite measurements, data that are not affected by clouds, such as the Global Telecommunication System (GTS) conventional data, can have a greater impact on the assimilation. In this study, we conducted experiments to examine which thresholds can be used to improve the microwave sounder radiance

TABLE 1. AMSU-A and ATMS channels and characterizations. Numbers in italics indicate the channels assimilated. ATMS channels in bold indicate the channels used for ATMS_T.

Frequency (GHz)	Channel		Beamwidth (°)		Characterization and peak WF (hPa)
	AMSU-A	ATMS	AMSU-A	ATMS	
23.8	1	*1*	3.3	5.2	H_2O, surface
31.4	2	*2*	3.3	5.2	H_2O, surface
50.3	3	***3***	3.3	2.2	Temperature sounding, surface
51.76		***4***		2.2	Temperature sounding, 950
52.8	4	***5***	3.3	2.2	Temperature sounding, 850
53.596 ± 0.115	5	***6***	3.3	2.2	Temperature sounding, 700
54.4	*6*	***7***	3.3	2.2	Temperature sounding, 400
54.94	7	***8***	3.3	2.2	Temperature sounding, 250
55.5	*8*	***9***	3.3	2.2	Temperature sounding, 200
57.29	*9*	***10***	3.3	2.2	Temperature sounding, 100
57.29 ± 0.217	*10*	***11***	3.3	2.2	Temperature sounding, 50
57.29 ± 0.322 ± 0.048	*11*	***12***	3.3	2.2	Temperature sounding, 25
57.29 ± 0.322 ± 0.022	*12*	***13***	3.3	2.2	Temperature sounding, 10
57.29 ± 0.322 ± 0.010	*13*	***14***	3.3	2.2	Temperature sounding, 5
57.29 ± 0.322 ± 0.0045	14	15	3.3	2.2	Temperature sounding, 2
89.0	15		3.3		H_2O sounding, surface
88.2		*16*		2.2	H_2O sounding, surface
165.5		*17*		1.1	H_2O sounding, surface
183.31 ± 7.0		*18*		1.1	H_2O sounding, 800
183.31 ± 4.5		*19*		1.1	H_2O sounding, 700
183.31 ± 3.0		*20*		1.1	H_2O sounding, 500
183.31 ± 1.8		*21*		1.1	H_2O sounding, 400
183.31 ± 1.0		*22*		1.1	H_2O sounding, 300

assimilation for TC forecasts by using the collocated MODIS and VIIRS cloud products.

2. Data

a. Microwave sounders

AMSU-A is a multichannel scanning radiometer with 15 channels at microwave frequencies ranging from 23.8 to 89.0 GHz. It scans across the satellite track at 30 viewing angles covering ±48.95° with a nominal FOV of 3.3° (48 km at nadir) (Diak et al. 1992; Weng et al. 2003). ATMS is a cross-track temperature/humidity sounder with 22 channels in bands from 23.8 to 183.3 GHz. It includes most channels of the AMSU-A and AMSU-B sensors plus new channels at 51.76 and 165.5 GHz. It has three antenna beamwidths of 1.1°, 2.2°, and 5.2° providing spatial resolutions of 16, 32, and 75 km at nadir, respectively (Muth et al. 2005). The beamwidths of ATMS are narrower than those of the AMSU-A channels, except for two channels at 23.8 and 31.4 GHz. Details of the AMSU-A and ATMS channel characteristics are listed in Table 1 (Diak et al. 1992; Weng et al. 2003; Muth et al. 2005).

b. High spatial resolution imager cloud products

MODIS onboard the *Terra* and *Aqua* platforms has 36 broadband spectral bands covering a range from 0.4 to 14.4 μm. Daily global cloud products with a high spatial resolution of 1 km are retrieved by combining the observed IR and visible radiances (King et al. 2003; Platnick et al. 2003). The MODIS cloud products include CM (Ackerman et al. 1998), cloud classification mask (Li et al. 2003; Li et al. 2007), cloud phase (Strabala et al. 1994), effective cloud-particle radius, cloud optical thickness (COT) (Nakajima and King 1990), and cloud-top properties (Baum et al. 2012). The MODIS CM algorithm is mainly based on the IR T_B thresholds and difference tests using the 3.9-, 8.6-, 11-, and 12-μm channels (Ackerman et al. 1998). In addition to the four channels, the H_2O and CO_2 absorption bands, near-IR, and visible channels are used in some cases, such as areas with cirrus and extremely high or low clouds. This MODIS CM algorithm can operate in near–real time with limited computer storage. Since the MODIS IR channels are primarily used to detect clouds, the MODIS CM is retrieved for day and night.

The VIIRS instrument on JPSS *Suomi-NPP* is a visible–IR sensor with 16 moderate-resolution channels (750 m at nadir), five imaging resolution channels (375 m at nadir), and a day/night band (DNB) (750 m across full scan) (Lee et al. 2006). It also provides high spatial resolution cloud products containing CM (Hutchison et al. 2005; Godin 2014a), cloud phase (Pavolonis and Heidinger 2004), cloud-top parameters (Baker 2012), COT, and effective

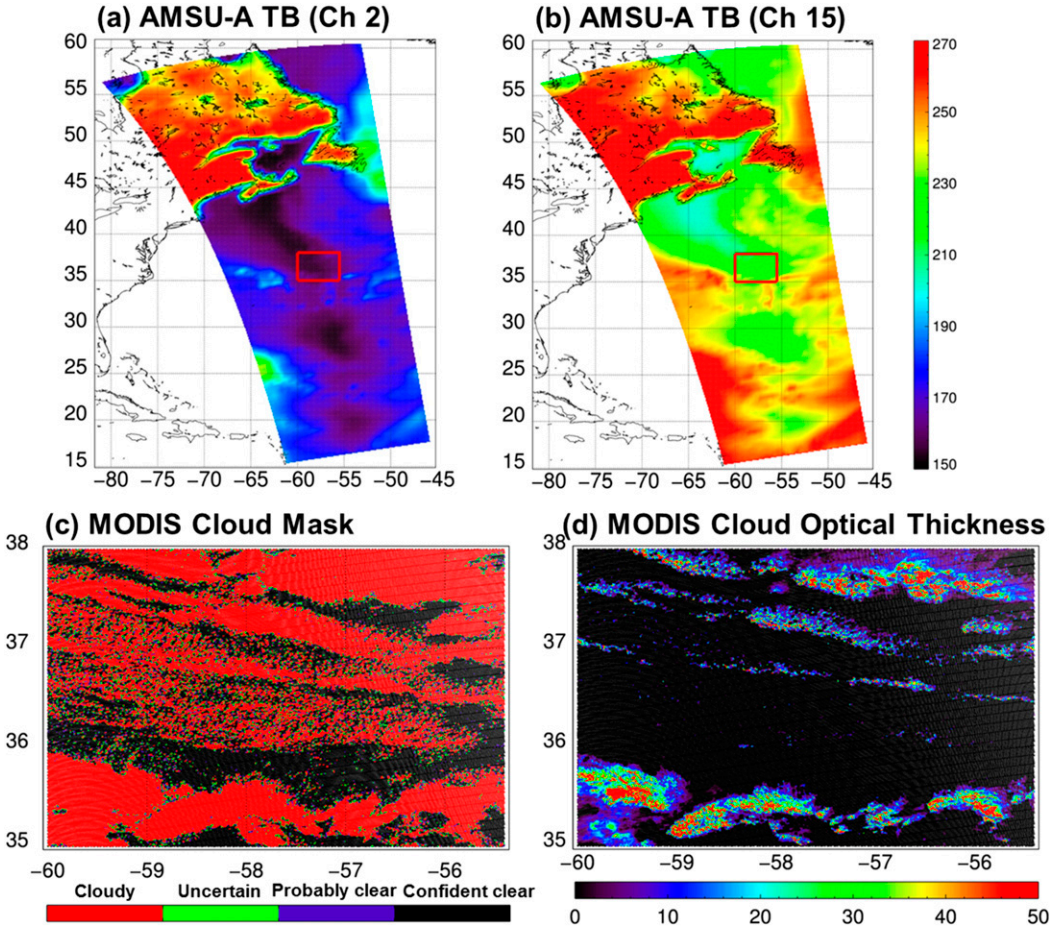

FIG. 1. AMSU-A T_Bs (K) at (a) 31.4- and (b) 89.0-GHz spectral channels observed at 1700 UTC 25 Oct 2012. (c) MODIS CM and (d) COT in the red box area in (a),(b).

radius (Godin 2014b). The VIIRS CM technique was developed using previous algorithms, and most closely follows the construction of the MODIS algorithm (Ackerman et al. 1998; Godin 2014a). The VIIRS COT retrieval process begins with determining the cloudy pixels and cloud phase via the VIIRS CM algorithm. For ice and water cloud phases, it uses visible and IR algorithms. The visible algorithms are applied for daytime retrievals. These algorithms use a set of precomputed reflectance lookup tables of the visible and near-IR bands, including the 1.61-, 0.672-, and 1.24-μm channels. The COT of daytime clouds is provided by the solar algorithms that determine COT by minimizing the error with respect to the sensor measured reflectances. The IR approach utilizes various combinations of radiances of the VIIRS 3.7-, 8.55-, 10.7625-, and 12.013-μm channels to infer cloud-top temperature and IR emissivity. Then the COT is determined by inversion of the parameterization equations in relation to cloud-top temperature, emissivity, and sensor measure radiance. (Reed 2013).

By taking advantage of the high spatial resolution imager cloud products, detecting cloud-affected radiances for measurements from relatively low-resolution microwave sounder measurements, such as AMSU-A and ATMS, can be derived. These parameters are useful for cloudy data QC in assimilating TC forecasts.

3. Methodology

Figure 1 shows the AMSU-A T_Bs at 31.4 and 89.0 GHz of a single granule, the MODIS CM and COT. The T_Bs in the red box are relatively lower than for other areas, providing no evidence of clouds in the box. However, the MODIS cloud products show that a large portion of the box is contaminated with small but relatively thick clouds that have COT of about 50 as shown in Fig. 1d. This comparison implies that the AMSU-A spatial resolution of 48 km at nadir is not enough to find differences between broken cloud and clear areas, and cloud-contaminated microwave FOVs

can be detected by using the high spatial resolution cloud product.

The collocation between AMSU-A/*Aqua* (hereafter AMSU-A) and MODIS/*Aqua* (hereafter MODIS) is constructed using the viewing geometry of AIRS, also on board the *Aqua* satellite. The FOVs of AMSU-A are approximately 3 times larger than those of AIRS, and it results in an AMSU-A FOV encompassing 9 AIRS FOVs arranged in a 3×3 matrix. Based on this scan geometry, the National Aeronautics and Space Administration (NASA) operationally generates AIRS Standard Retrieval Products combining IR/MW measurements. Since the MODIS–AIRS collocation methodology was already developed by Nagle (1998), MODIS pixels within an AIRS FOV are collected using this method. Then an AMSU-A FOV with the MODIS cloud products are collocated by simply matching an AMSU-A FOV with the MODIS pixels mapped inside the corresponding nine AIRS FOVs on the assumption that the gaps between the nine AIRS FOVs may be disregarded. Measurements of ATMS and VIIRS on board the *Suomi-NPP* are collocated based on the method established by Nagle and Holz (2009). The data preprocessing time for collocating a microwave sounder granule with cloud products from the imager is less than 2.5 min using Linux CentOS, version 6.6, with 16 Intel Xeon E5-2690 CPUs at 2.9 GHz.

Cloud-contaminated microwave radiances are detected using CF thresholds without information about cloud types. The MODIS and VIIRS CM are used to calculate the CF of AMSU-A and ATMS FOVs, respectively, then cloudy microwave FOVs are detected using various CF thresholds. The MODIS CM algorithm combines IR and visible techniques to determine the four levels of confidence (''cloudy,'' ''uncertain,'' ''probably clear,'' and ''confident clear'') with regard to whether a pixel is clear or cloudy (Ackerman et al. 1998, 2010). In this study, MODIS pixels flagged as cloudy or uncertain are considered cloudy pixels. The CF of an AMSU-A FOV is then calculated as the ratio of the number of MODIS cloudy pixels to the total number of collocated MODIS pixels within an AMSU-A FOV. The VIIRS CM retrieval technique produces a cloud confidence for each moderate resolution of VIIRS pixel with the same four levels as the MODIS CM (Ackerman et al. 1998, 2010; Godin 2014a). A similar process is used to calculate the ATMS CF. ATMS FOVs are collocated with the VIIRS CM and then the CF of each ATMS FOV is calculated. Using the CF of AMSU-A and ATMS from the collocated high-resolution imager CM, assimilation experiments are carried out to understand the advantage of subpixel cloud detection for radiance assimilation and TC forecasts.

4. Data assimilation system and experiment design

a. Tropical cyclones

To investigate the impact of cloud-contaminated microwave sounder radiances on TC forecasts, microwave measurements collocated with imager cloud products are assimilated into NWP for two TC cases. In this study, Hurricane Sandy (2012) and Typhoon Haiyan (2013), which were their season's most devastating and strongest TCs, are selected for the assimilation and forecast experiments (Joint Typhoon Warning Center 2013; Stewart 2014).

Hurricane Sandy formed on 22 October 2012 in the western Caribbean Sea. It intensified while moving steadily to the north, with the National Hurricane Center (NHC) upgrading it to hurricane status on 24 October. After passing eastern Cuba, the hurricane quickly weakened as it moved through the Bahamas. However, it restrengthened into a hurricane while it was moving northeastward. The track of Sandy bent to the northwest toward the mid-Atlantic states early on 29 October, and reached a second peak of intensity near 1200 UTC. By 2100 UTC 29 October, Sandy became extratropical and the center of Posttropical Cyclone Sandy made landfall at about 2300 UTC near Brigantine, New Jersey. Damage in the United States was estimated at nearly $50 billion, and at least 147 direct deaths were recorded across the Atlantic basin due to Sandy (Blake et al. 2013).

Haiyan was the last typhoon of 2013 in the western North Pacific basin. It formed from south of Pohnpei Island on 2 November 2013 and then proceeded quickly westward toward Micronesia. On 4 November, the Japan Meteorological Agency upgraded this system to a tropical storm and assigned it the name Haiyan. About 1800 UTC 7 November, it reached a maximum intensity of 87.5 m s^{-1} with a central pressure estimated at 895 hPa. It was the highest wind speed ever reported for a TC by the Joint Typhoon Warning Center. Several hours later, continuing on a west-northwestward track, it made landfall close to the city of Tacloban in the central Philippines on 8 November (Lander et al. 2014). As of 3 April 2014, 6293 individuals were reported dead, 1061 missing, and 28 689 injured in the Philippines region (National Disaster Risk Reduction and Management Council 2014).

b. Assimilation system and forecast model

AMSU-A and ATMS measurements are separately assimilated into a forecast model through the National Oceanic and Atmospheric Administration (NOAA) community GSI, version 3.3, analysis system. GSI is a unified three-dimensional variational (3DVAR) data assimilation system for both global and regional applications and was initially developed by NCEP as a next-generation analysis

system based on the operational Spectral Statistical Interpolation scheme (Wu et al. 2002; Kleist et al. 2009). The GSI incorporates a fast radiative transfer model, the Community Radiative Transfer Model (CRTM) developed by the Joint Center for Satellite Data Assimilation (JCSDA), allowing direct assimilation of satellite-observed radiances (Han et al. 2006; Chen et al. 2008). The CRTM simulates radiances from a large number of sensors on board satellites covering the microwave, IR, and visible spectral regions. As mentioned above, the GSI QC function detects cloud-affected microwave radiances using SI and cloud liquid water path thresholds (Hu et al. 2014). Since the SI and liquid water path are calculated based on the observed radiance and its deviation from the background status, performance of the QC system depends on the accuracy of CRTM simulations, background status, and the empirical function for the liquid water path. For the AMSU-A and ATMS QC, simulated and observed T_Bs at 23.8, 31.4, 52.8, and 54.4 GHz are mainly used to estimate SI and cloud liquid water path.

The Weather Research and Forecasting (WRF) Model is a next-generation mesoscale NWP system designed to serve both atmospheric research and operational forecasting needs (Skamarock et al. 2008). WRF, version 3.2.1, was employed as the NWP model to provide TC track and intensity forecasts in this study. The WRF single-moment 6-class microphysics scheme (Hong and Lim 2006) and the Kain–Fritsch cumulus parameterization scheme (Kain 2004) are used for cloud-resolving simulations. The Yonsei University planetary boundary layer scheme was selected to state the lowest part of the atmosphere (Hong et al. 2006).

c. *Experimental design*

A computational domain for the Sandy forecast was set up with 400 × 350 horizontal points at a 12-km grid distance and 35 vertical levels from the surface to 10 hPa. The horizontal domain covers an area of 5°–50°N and 40°–100°W on the Lambert Conformal Conic projection as shown in Fig. 2. Since the assimilation scheme was designed to run at 6-h cycles followed by a 72-h forecast, the model is performed with 8 assimilation cycles from 0600 UTC 25 October to 0000 UTC 27 October 2012, and the forecast period is from 0600 UTC 25 October to 0000 UTC 30 October 2012. This study follows the Global Forecast System (GFS) operational setting for thinning boxes and uses the same channels as the operational model. AMSU-A radiances at 7 channels (channels 6, 8, 9, 10, 11, 12, and 13) and ATMS measurements at 21 channels (channels 1–14 and 16–22) are assimilated into the assimilation system, and the thinning boxes for AMSU-A and ATMS are 60 and 120 km, respectively. The channels were selected based on the features of the channels and long-term tests for GFS operational assimilation. The thinning box size depends on the spatial resolution of the instruments. The lowest nadir resolution of ATMS is about 75 km (channels 1 and 2) while AMSU-A has a spatial resolution of 48 km at nadir. This dissimilarity in the spatial resolution may result in different thinning boxes between AMSU-A and ATMS. A ±90-min assimilation time window was applied for the Sandy experiments. The background error covariance matrix and observation error table follow the North American Mesoscale Forecast System (NAM), and the NCEP operational regional system. The initial bias coefficients are from the NCEP GFS, and the bias correction coefficient is updated based on the previous results with the cycling run.

Details of the experimental design for the Typhoon Haiyan assimilation and forecast are similar to those for Hurricane Sandy, except for the following changes. The model domain of 540 × 300 horizontal grid points extends from 5°S, 100°E to 30°N, 160°E covering the federated states of Micronesia, the Philippines, and the Guangxi Province in southeastern China. The assimilation time is from 0600 UTC 4 November to 0000 UTC 7 November 2013, and a ±150-min assimilation time window was used to allow more observations during the genesis of Haiyan. The longer window accepts more AMSU-A and ATMS measurements, and increases the impact of the radiance assimilation. On the other hand, uncertainties caused by weather variation could also be included in the assimilation process due to the longer window. Instead of the NAM as used for Hurricane Sandy, background error covariances and observation errors based on the NCEP GFS were used for the Typhoon Haiyan experiment.

In addition to the AMSU-A and ATMS radiances, data from the World Meteorological Organization (WMO) GTS is assimilated into the system. This includes all conventional data, such as surface observations, radiosondes, aircraft data, and wind profiles derived from radar and satellite. The initial conditions and boundary conditions come from the NCEP Final Operational Global Analysis data. Experiments are carried out with various CF thresholds in addition to the default cloud screening algorithm in the current GSI system. It is important to note that the subpixel cloud detection using the high spatial resolution cloud products is followed by the GSI default cloud screen.

5. Results and analysis

a. *Hurricane Sandy*

Radiances observed from AMSU-A and ATMS are separately assimilated into the system. The forecast

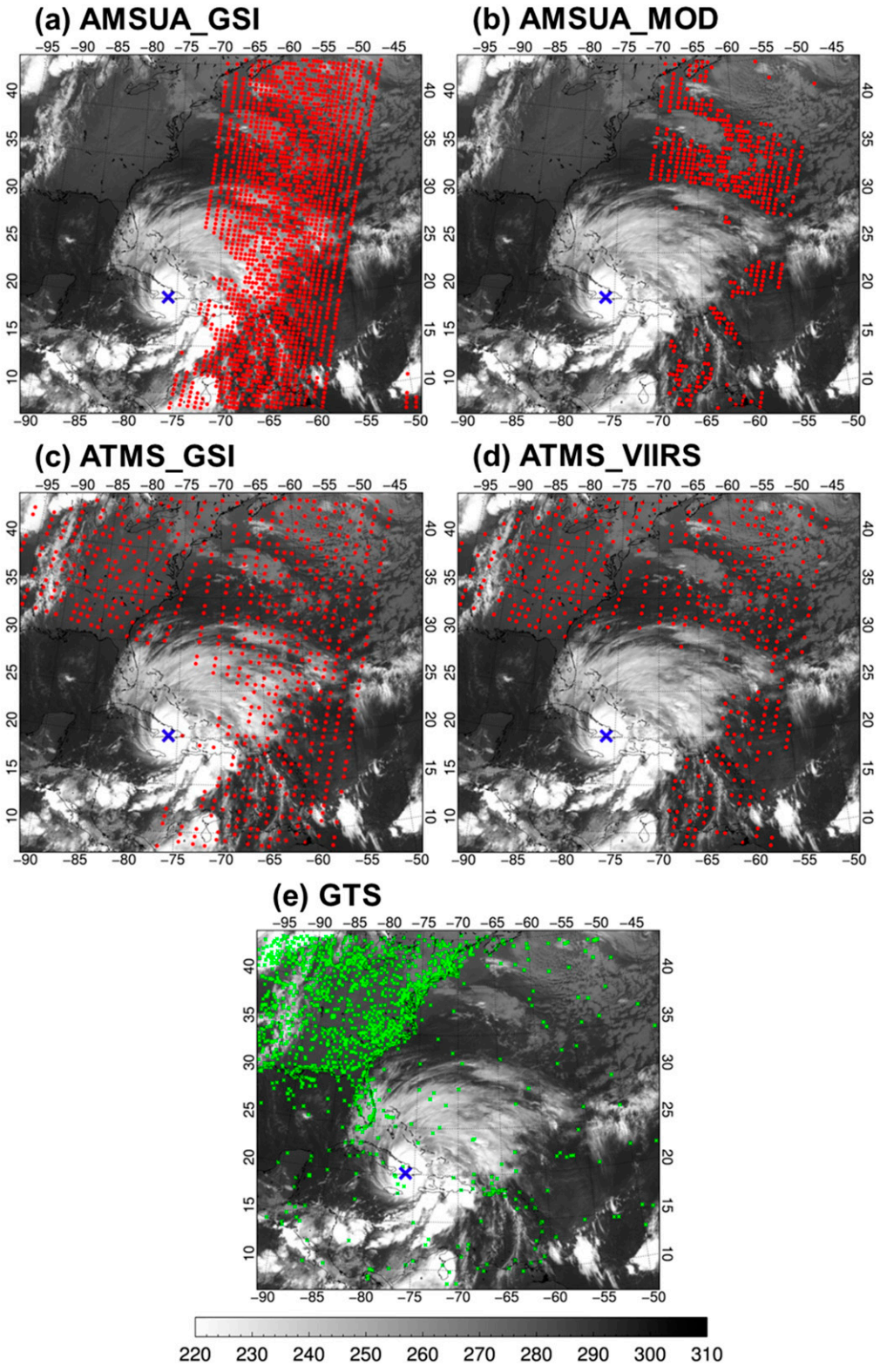

FIG. 2. The coverages of the assimilated microwave measurements at 54.4-GHz spectral channel shown as red lines for (a) AMSUA_GSI, (b) AMSUA_MOD, (c) ATMS_GSI, and (d) ATMS_VIIRS along with (black and white) *GOES-13* T_Bs (K) at 11 μm. Microwave radiances in these coverages are assimilated into the GSI system for the Hurricane Sandy experiments at 0600 UTC 25 Oct 2012 analysis time. The blue $\times$ symbols indicate the center of Hurricane Sandy. (e) The locations of the assimilated GTS conventional data are plotted with green crosses.

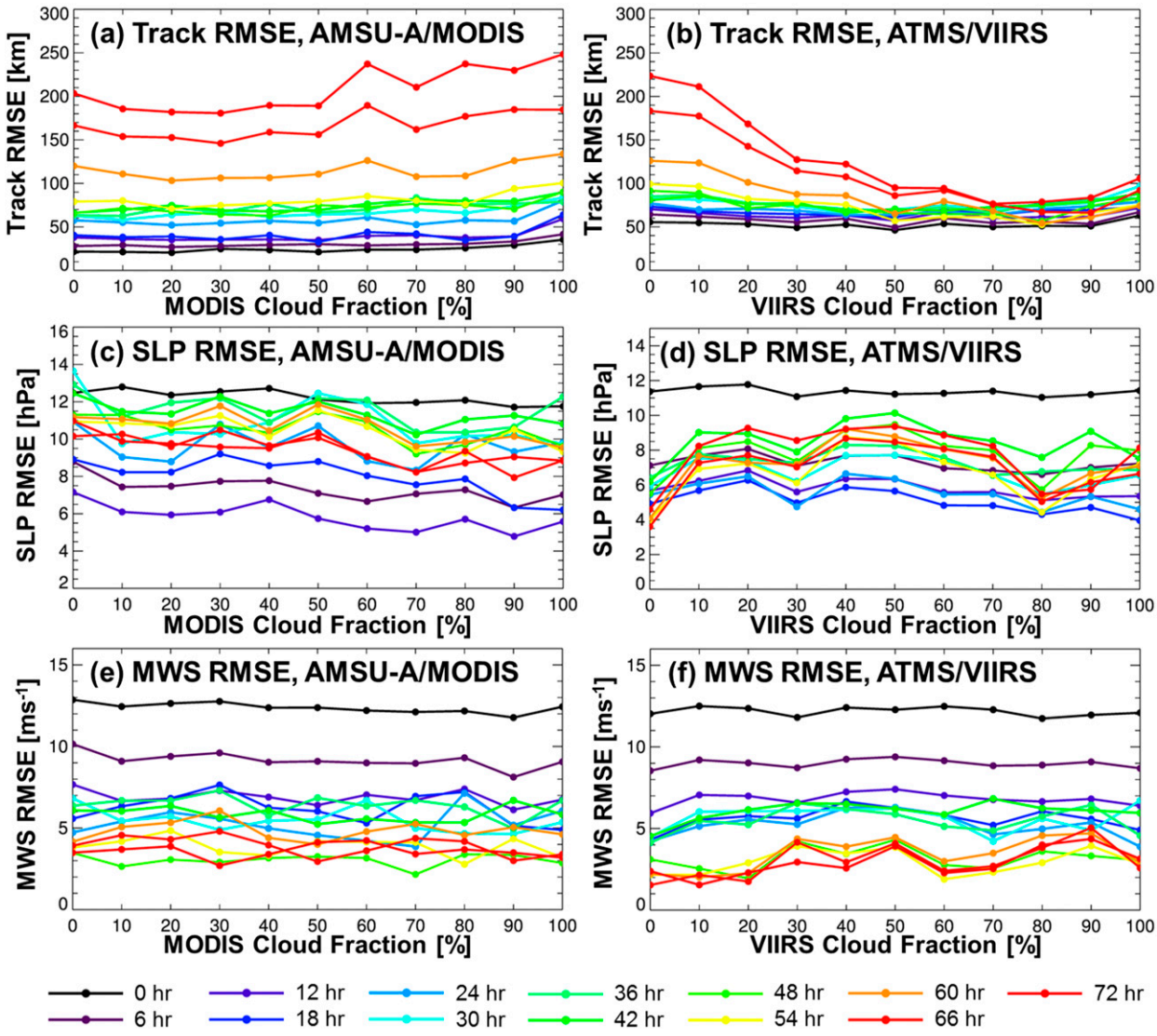

FIG. 3. (a),(b) The track; (c),(d) SLP; and (e),(f) MWS RMSEs for various CF thresholds for the Hurricane Sandy experiments using (a),(c),(e) AMSU-A/MODIS and (b),(d),(f) ATMS/VIIRS CM products. The color legend shows the forecast times.

root-mean-square errors (RMSEs) of the hurricane track, minimum sea level pressure (SLP), and maximum surface wind speed (MWS) are shown in Fig. 3 for various CF thresholds. The RMSEs are calculated from forecasts at eight different starting times since the model is performed with eight assimilation cycles. The reference track, SLP, and MWS are obtained from the NHC best-track dataset. The abscissa of the figure is the upper limit of the CF of the assimilated AMSU-A or ATMS data. For example, a CF threshold of 50% means that microwave measurements from FOVs with CF less than 50% within each FOV are assimilated in the system. The track RMSE of the AMSU-A experiments are plotted in Fig. 3a for the various forecast times from 0 to 72 h. For short lead forecast times between 0 and 48 h, the range of variation in RMSE is relatively small to show the impact of different CF thresholds. Conversely, the greater dynamic ranges of RMSE are shown for the longer lead-time forecasts between 54 and 72 h, where the improvements are actually needed. The track RMSEs of the longer lead forecast times decrease with an increasing CF threshold up to around 20%–30%, but thereafter, it increases and reaches its maximum at a CF of 100%. The minimum values of the track RMSE for the forecast times of 60, 66, and 72 h are 103.2, 146.0, and 180.7 km, respectively; these are found at the CF thresholds of 20% and 30%. As in the case of the AMSU-A track error, the track RMSE of the ATMS assimilation experiment in

Fig. 3b also shows a strong association with the VIIRS CF threshold. However, the CF thresholds of the minimum track errors are found between 70% and 90%, which is larger than that of the AMSU-A experiments. The RMSEs for the 60-, 66-, and 72-h forecasts have minimum RMSEs of 54.2, 66.4, and 76.4 km at the CFs of 80%, 90%, and 70%, respectively. The curves of the track RMSEs in Figs. 3a and 3b indicate that the cloud screening algorithm in the current GSI system (identical to a CF threshold of 100%) is not sufficient, and the subpixel cloud detection using the MODIS and VIIRS CF can improve the track forecast by balancing the data usage and the reduction in cloud contamination. The SLP RMSEs of the AMSU-A and ATMS experiments are given in Figs. 3c and 3d, respectively. The minimum SLP RMSEs are found between 70% and 90% for 10 forecast times of the total 13 forecast times for the AMSU-A experiments. The smallest SLP RMSE of the 72-h forecast, 8.2 hPa, is located at 70%. For the ATMS SLP error, although the RMSE varies with the VIIRS CF thresholds, it is hard to find a definitive trend in the SLP error by increasing or decreasing the CF threshold. Similarly, the correlations between the MWS RMSEs and the CF threshold are not clear unlike the track error. Comparing with the close relation between the track RMSE and the CF threshold, the SLP and MWS RMSEs show a less significant association with the CF threshold.

As shown in Table 1, AMSU-A is mainly composed of the temperature-sounding channels while ATMS has O_2 and H_2O absorption bands in the spectral region of 50.3–58.3 and 183.3 GHz, respectively. The Humidity Sounder for Brazil (HSB), an instrument on board *Aqua*, has four channels between 150 and 190 GHz. However, the HSB ceased operation on February 2003 due to a mirror scan motor failure (Olsen 2005), and measurements in the H_2O absorption bands from *Aqua* are no longer available. The differences between the AMSU-A and ATMS channels used are in the low-level temperature channels and humidity-sounding channels in the spectral region of 23.8–53.6 GHz and around 183.3 GHz, respectively. Considering the large observational variances of the ATMS surface viewing channels (channels 1–4) of the GSI operational setting, it is expected that the peak difference between the AMSU-A and ATMS experiments in Figs. 3a and 3b is primarily due to the ATMS humidity-sounding channels. To assess the impact of the humidity-sounding channels on the assimilation, a sensitivity test is performed using only the ATMS temperature-sounding channels (hereafter ATMS_T).

Radiances from the 12 ATMS channels in the O_2 absorption band, channels 3–14, are assimilated into the system for various VIIRS CFs, and the calculated hurricane track RMSEs are given in Fig. 4a. Unlike the track RMSE of the ATMS experiments in Fig. 3b, the track error of ATMS_T rapidly decreases with an increasing CF threshold between 0% and 30%. The minimum track errors are shown near the CF threshold of 30%, which is closer to that of the AMSU-A experiment rather than that of the ATMS experiment. The large discrepancy in track RMSE between the ATMS and ATMS_T experiments stems from the humidity-sounding channels of ATMS.

To explain the different CF thresholds for the minimum track errors between the ATMS and ATMS_T experiments, analysis fields from the ATMS_T experiments with the default GSI cloud screening algorithm (hereafter ATMS_T_GSI) and with CF $<$ 30% (hereafter ATMS_T_VIIRS) and analysis fields from the ATMS experiment with CF $<$ 80% (ATMS_VIIRS) are compared with radiosonde temperature and moisture profiles. The radiosonde locations are given in Fig. 5. Approximately 30–35 radiosondes are available at one analysis time at each pressure level. Temperature and moisture profiles from an available radiosonde are collocated with spatially interpolated profiles from the three nearest grids of analysis fields, and then the mean bias and RMSE are calculated. The maximum distance between radiosondes and collocated profiles from analysis fields is the grid distance, 12 km. Since radiosonde observations are available every 6 h from 0000 UTC, temporal interpolation is not performed. Figures 4b–e show the temperature and moisture mean bias and RMSE. Compared to the ATMS_T_GSI, the temperature mean bias and RMSE of the ATMS_T_VIIRS increased above 350 hPa, while there seems to be little difference below 350 hPa. The discrepancies in temperature statistics between the ATMS_T_VIIRS and ATMS_T_GSI are about 0.21 and 0.23 K for the mean bias and RMSE, respectively, near a pressure level of 270 hPa. For the moisture analysis, the mean bias and RMSE of the ATMS_T_VIIRS decreased below 500 hPa with improvements up to 0.09 and 0.14 g kg^{-1}, respectively. The comparison between ATMS_T_VIIRS and ATMS_T_GSI indicates that the subpixel cloud detection affects the moisture analysis field as well as the temperature even though only the temperature-sounding channels are used in the assimilation. The improvement in the moisture field of ATMS_T_VIIRS, however, is relatively small compared to the experiment using all the ATMS channels, ATMS_VIIRS. The black dotted lines in Figs. 4d and 4e for the ATMS_VIIRS show that the use of the humidity-sounding channels considerably reduces the mean bias and RMSE of the moisture profiles. Since absorption by the water vapor continuum around 50.3–58.3 GHz is smaller than that of the 183-GHz water vapor absorption band, more strict cloud screening thresholds

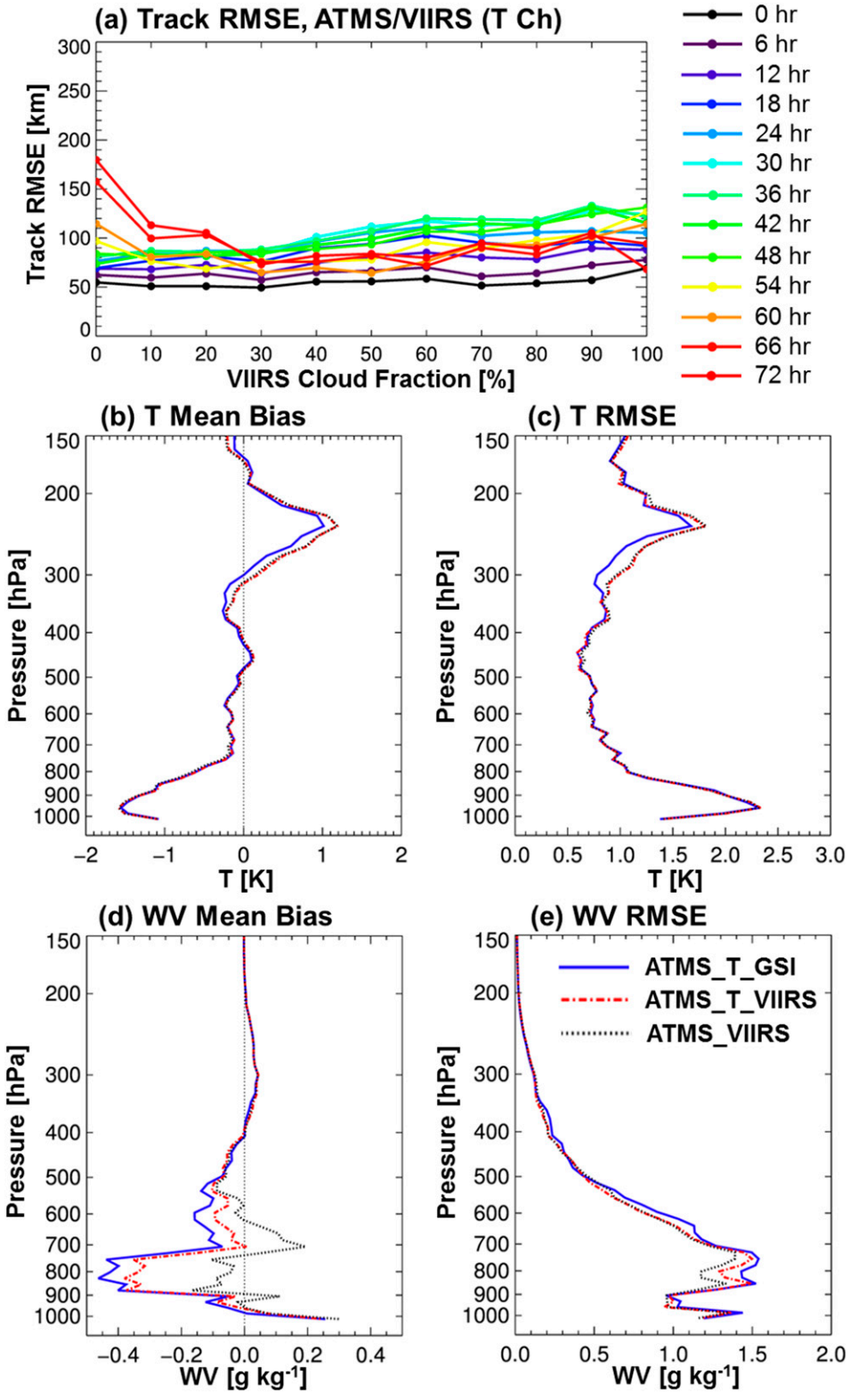

FIG. 4. (a) The track RMSEs for various CF thresholds for the Hurricane Sandy experiments for ATMS_T. (b),(d) Mean biases and (c),(e) RMSEs for (b),(c) temperature and (d),(e) moisture profiles of the analysis fields. The statistics are calculated against the radiosondes for ATMS_T_GSI (blue solid line), ATMS_T_VIIRS (red dashed–dotted line), and ATMS_VIIRS (black dotted line).

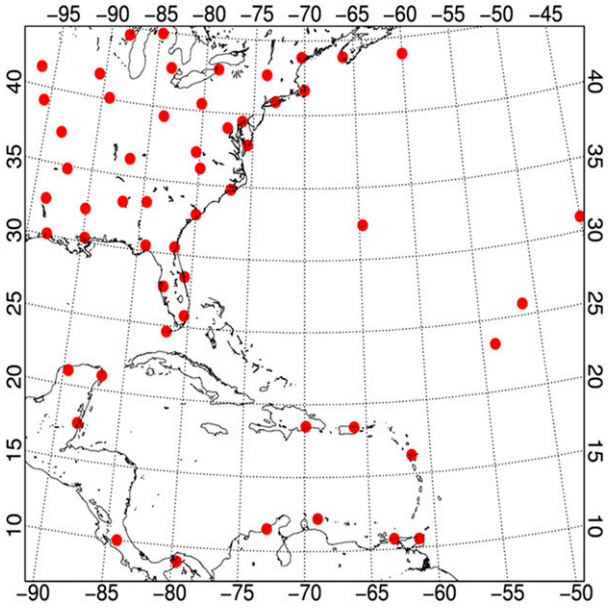

FIG. 5. The locations of the radiosondes that are compared with the analysis fields.

are required to distinguish the absorption by water vapor from an impact of clouds on radiances in this spectral region. From the above, it is apparent that the different CF thresholds of the minimum track errors between the AMSU-A and ATMS experiments come from the different spectral channels of the instruments.

Based on the RMSE analysis for various CF thresholds in Fig. 3, optimal CF thresholds, CF $<$ 70% for the AMSU-A experiments and CF $<$ 80% for the ATMS experiments, were determined after considering the track, SLP, and MWS errors. The coverages of the assimilated AMSU-A radiances for the experiments using the AMSU-A stand-alone cloud detection (hereafter AMSUA_GSI) and the AMSU-A/MODIS cloud detection with a CF threshold of 70% (hereafter AMSUA_MOD) at the first assimilation time are shown in Figs. 2a and 2b, respectively, along with *GOES-13* T_Bs at 11 μm. The plotted coverages are for the AMSU-A measurements in channel 6 (54.4 GHz), which has a weighting function peaking at approximately 400 hPa. About 92% and 25% of the AMSU-A measurements over the model domain are assimilated for the AMSUA_GSI and AMSUA_MOD, respectively, at the 0600 UTC 25 October 2012 analysis time. Considering the AMSU-A FOVs within a 1000-km radius from the TC center, AMSUA_MOD eliminates about 99.2% of the observations while the AMSUA_GSI allows 53.8% of the AMSU-A measurements to be assimilated. It indicates that cloudy FOVs adjacent to the TC center are screened out by the subpixel cloud-detection method, and most of the rejected data are within this area. Discrepancies in coverage between the two cloud-detection algorithms are found mainly around Hurricane Sandy over the North Atlantic Ocean and the Caribbean Sea, where heavy rainfall is generally expected. Figures 2c and 2d display the data coverages of the ATMS measurements at channel 7 (54.4 GHz) with the GSI default cloud detection (hereafter ATMS_GSI) and the subpixel cloud detection (hereafter ATMS_VIIRS), respectively. The assimilated ATMS measurements in Figs. 2c and 2d are more sparsely scattered than the AMSU-A radiances in Figs. 2a and 2b due to the large thinning box. Approximately 95% of ATMS radiances are eliminated by the thinning process. The coverages below 35°N are very similar to those of the AMSU-A experiments, which were covered by thick and homogeneous clouds associated with Hurricane Sandy. The AMSUA_MOD and ATMS_VIIRS coverages are different over the northeast corner of the AMSU-A granule; relatively low and small broken clouds are observed in this region, in contrast to the area south of 35°N. The discrepancy in this area is likely related to the difference in the instruments' spatial resolution. The resolution of ATMS at channel 7 is about 32 km at nadir while AMSU-A channel 6 has a FOV size of 48 km. Obviously, the higher ATMS resolution facilitates more detailed cloud detection particularly for small clouds as shown in this area. AMSU-A radiances measured over North America are not assimilated, since those are measured after the assimilation window of 0430–0730 UTC, while the ATMS measurements are available.

The locations of the assimilated GTS data are plotted in Fig. 2e. A total of 14 388 conventional data observed at 2060 locations are assimilated into the system for the first analysis field, regardless of the presence of clouds. Some of the data are located over the hurricane, the area flagged as clouds by the subpixel cloud-detection method. Over the cloudy area, it is expected that the GTS data are allowed to have a greater impact on the analysis by eliminating cloud-contaminated radiances using the subpixel cloud-detection method.

To understand the impact of the AMSU-A/MODIS cloud detection on the thermodynamic status of the atmosphere, the temperature and water vapor analysis differences at 500 hPa between the AMSUA_MOD and AMSUA_GSI analysis fields at 0600 UTC 25 October 2012 are displayed in Figs. 6a and 6d. In this study, the assimilated AMSU-A radiances are observed at spectral channels within the O_2 absorption spectrum. For the ATMS experiments, on the other hand, radiances from both the O_2 and water vapor absorption channels are assimilated into the system. Consequently, it is expected that the assimilation of the AMSU-A measurements has less influence on the moisture field compared to that of

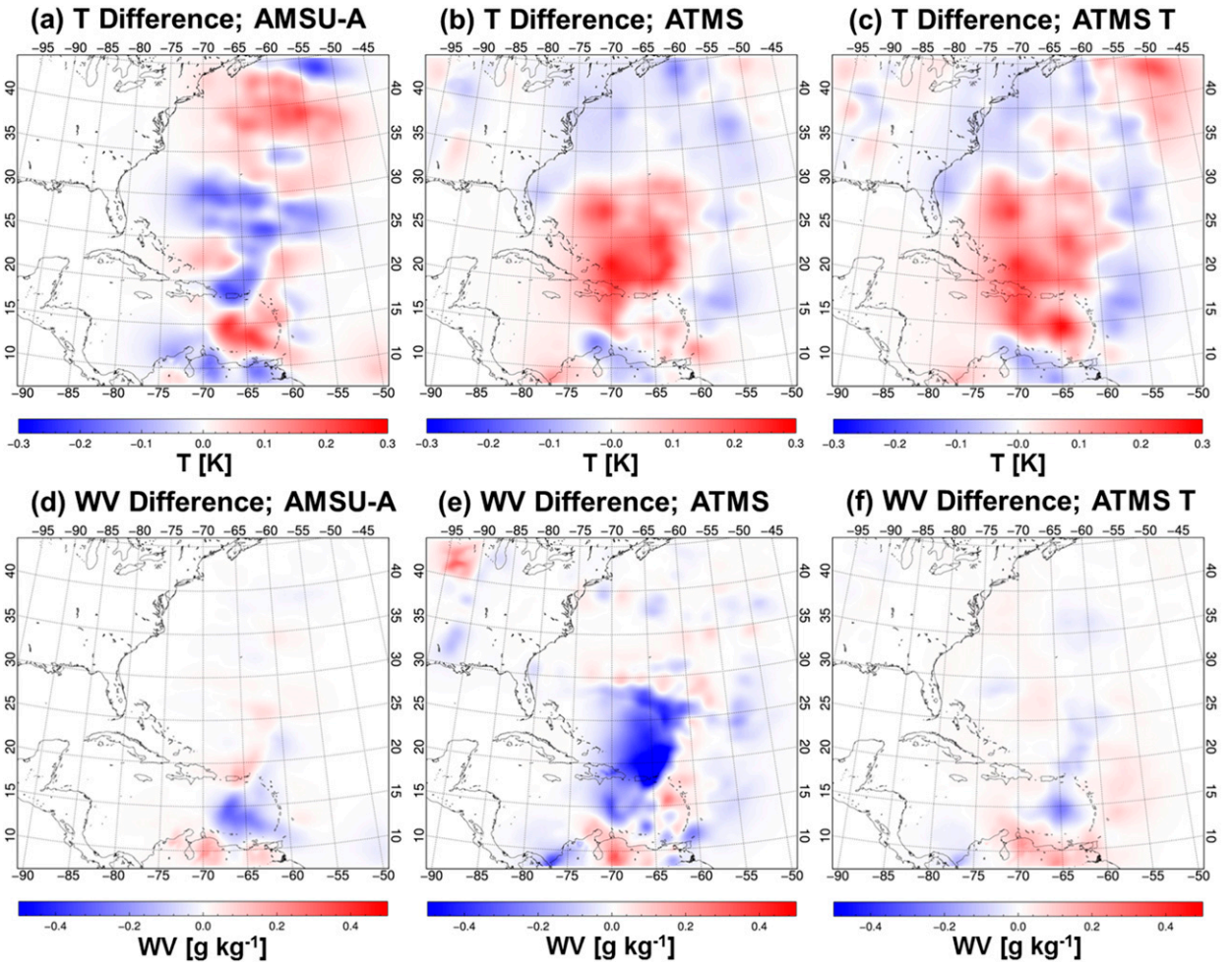

FIG. 6. The analysis field differences in (a)–(c) temperature and (d)–(f) water vapor mixing ratio at 500 hPa for the Hurricane Sandy experiments. (a),(d) The difference between AMSUA_MOD and AMSUA_GSI (AMSUA_MOD − AMSUA_GSI); (b),(e) the difference between the ATMS_VIIRS and ATMS_GSI (ATMS_VIIRS − ATMS_GSI); and (c),(f) the difference between the ATMS_T_VIIRS and ATMS_T_GSI (ATMS_T_VIIRS − ATMS_T_GSI) at 0600 UTC 25 Oct 2012.

the ATMS experiments. The temperature difference between AMSUA_MOD and AMSUA_GSI is shown over the entire AMSU-A coverage area and reaches up to ±0.25 K. The temperature change implies that the subpixel cloud detection has a substantial impact on the temperature analysis field. For the differences in water vapor mixing ratio, there are negative biases close to $-0.3\,\mathrm{g\,kg^{-1}}$ over the southern part of the domain. The change in the moisture field is, however, limited to only a part of the domain unlike the temperature field, and it seems that the analysis field change is dominated by the temperature from the AMSU-A experiment.

The temperature and moisture difference between ATMS_VIIRS and ATMS_GSI in Figs. 6b and 6e shows a marked distinction from the AMSU-A experiments. In contrast to the AMSU-A experiments, the obvious differences are found in the moisture field as well as the temperature field. If we take into account that the O_2 and H_2O absorption bands are assimilated into the ATMS experiment, it is reasonable that both temperature and moisture fields are affected by the different cloud-detection algorithms. The moisture field changed throughout the ATMS coverage, and noticeable negative biases are captured south of 30°N where the subpixel cloud-detection algorithm discards many of the ATMS measurements. These negative biases indicate the ATMS_VIIRS analysis is generally drier than the ATMS_GSI due to less cloud contamination. It can be explained in terms of the overestimation of the ATMS_GSI moisture field. Since both clouds and water vapor reduce transmittance of the atmosphere, misclassification of clouds as clear leads to an overestimation of the analysis field humidity, causing the negative biases in Fig. 6e. Another possible explanation is the high moisture

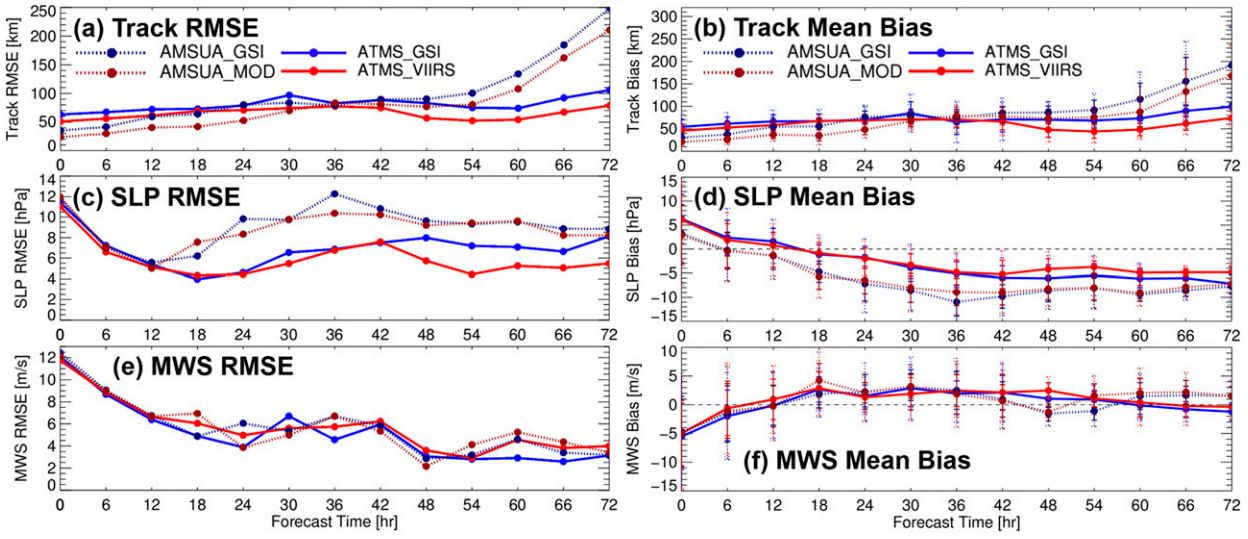

FIG. 7. (a),(b) The track; (c),(d) SLP; and (e),(f) MWS (a),(c),(e) RMSEs and (b),(d),(f) mean biases for the Hurricane Sandy forecasts for AMSUA_MOD (dark red dotted line), AMSUA_GSI (dark blue dotted line), ATMS_VIIRS (red solid line), and ATMS_GSI (blue solid line). Solid and dotted vertical bars in the right panels indicate the 80% and 95% confidence intervals of the mean biases, respectively.

content surrounding the hurricane. Within a 1000-km radius from the center, 98.7% of ATMS measurements are screened out by the subpixel cloud-detection method while the GSI default algorithm rejects 60% of the observations. The higher elimination ratio of ATMS_VIIRS around the hurricane center results in fewer assimilated ATMS measurements and a drier analysis field for ATMS_VIIRS accordingly. The temperature field is also considerably affected by the subpixel cloud detection over the entire ATMS coverage area. Since the ocean surface emissivity in the microwave spectral region sharply varies from 0.2 to 0.8 depending on the frequency (Svendsen et al. 1983; Hewison and English 1999), the T_Bs of cloudy FOVs are higher than those of clear FOVs at low-frequency channels and vice versa at high-frequency channels. Therefore, both positive and negative biases in the temperature field can be introduced by the subpixel cloud detection as shown in Fig. 6b. The effects of subpixel cloud detection on the temperature fields of AMSUA_MOD and ATMS_VIIRS are quite distinct from each other. It is highly probable that these differences stem from the low-level temperature-sounding channels of ATMS. An additional experiment indicates that the most dominant channel in the AMSU-A assimilation is channel 6 (54.4 GHz). For the ATMS assimilation experiments, otherwise, observations at 52.8 and 53.6 GHz (channels 5 and 6) have comparable influences to the radiances at 54.4 GHz (channel 7) on the temperature field. Moreover, the impacts of AMSU-A channel 6 and ATMS channel 7 show similarities in their spatial distribution while ATMS channels 5 and 6 display completely different patterns. Consequently, it is understandable to assume that the use of low-level temperature-sounding channels on ATMS results in the discrepancy of the temperature field difference in Figs. 6a and 6b. Analysis temperature and moisture field differences between ATMS_T_VIIRS and ATMS_T_GSI are also plotted in Figs. 6c and 6f, respectively, to help understand the influence of the H_2O absorption band. Without the humidity-sounding channels, the moisture field difference is dramatically reduced to between -0.38 and $0.08\,g\,kg^{-1}$, which is closer to that of AMSUA_MOD rather than ATMS_VIIRS. On the contrary, there is little difference in temperature fields between ATMS_VIIRS in Fig. 6b and ATMS_T_VIIRS in Fig. 6c.

The track, SLP, and MWS RMSEs and mean biases of the AMSUA_GSI, AMSUA_MOD, ATMS_GSI, and ATMS_VIIRS are plotted for various forecast times in Fig. 7. To represent the uncertainties in the mean biases, 80% and 95% confidence intervals are plotted with vertical bars in Figs. 7b, 7d, and 7f. Table 2 lists the details of the experiments. Comparing the RMSEs and mean biases from the GSI cloud detection and subpixel cloud detection (AMSUA_GSI vs AMSUA_MODIS and ATMS_GSI vs ATMS_VIIRS), it is evident that the track errors are reduced (maximum 38-km improvement in RMSE and 28-km improvement in mean bias) in forecast times when the cloud-contaminated radiances are rejected with the collocated high spatial resolution CF. The SLP errors of the subpixel cloud detection are overall smaller (maximum 2.8-hPa improvement in RMSE and 2.3-hPa improvement in mean bias) than those of the

TABLE 2. Description of the experiments and datasets used in this study.

TC	Expt	Data assimilated				Cloud-detection method (threshold)
		GTS	AMSU-A	ATMS	ATMS (Ch 3–14)	
Hurricane Sandy	AMSUA_GSI	O	O			GSI
	AMSUA_MOD	O	O			Subpixel (CF < 70%)
	ATMS_GSI	O		O		GSI
	ATMS_VIIRS	O		O		Subpixel (CF < 80%)
	ATMS_T_GSI	O			O	GSI
	ATMS_T_VIIRS	O			O	Subpixel (CF < 30%)
Typhoon Haiyan	AMSUA_GSI	O	O			GSI
	AMSUA_MOD10	O	O			Subpixel (CF < 10%)
	AMSUA_MOD90	O	O			Subpixel (CF < 90%)
	ATMS_GSI	O		O		GSI
	ATMS_VIIRS	O		O		Subpixel (CF < 80%)
	ATMS_COT	O		O		Subpixel (COT < 5)

GSI cloud detection as well, although slight degradations occur at some forecast times. For MWS, comparable results have been shown in the experiments, making it difficult to determine which is better.

The forecast errors from the experiments using AMSU-A are compared to those from the ATMS experiments. The track RMSE and mean bias of the AMSUA_GSI are slightly smaller than those of the ATMS_GSI prior to the 36-h forecast time. However, track errors sharply increase with the forecast time, and then reach the maximum values of 248.5 and 191.7 km in RMSE and mean bias, respectively, at the 72-h forecast. By contrast, the RMSE and mean bias of the ATMS_GSI barely reach 105.8 and 99.2 km, respectively, demonstrating a marked difference up to 142.7 km in RMSE from the AMSUA_GSI. The widths of the confidence intervals of the AMSUA_GSI and AMSUA_MOD rapidly increase after the 54-h forecast, compared to the ATMS experiments, which changed only slightly. It implies that the stability of the longer lead-time track forecast depends on which data are assimilated into the system.

For the SLP in Figs. 7c and 7d, the RMSEs and absolute mean bias from ATMS_GSI are lower than those from the AMSUA_GSI after the 12-h forecast time with the differences between 0 and 5.4 hPa in RMSE and 0 and 5.8 hPa in mean bias. The ATMS_VIIRS, as well as the ATMS_GSI, show smaller track and SLP RMSEs in comparison with those from the AMSUA_MOD (~131 km in track RMSE and ~5 hPa in SLP RMSE). The forecast errors in Fig. 7 provide evidence that the use of the subpixel cloud detection (red and dark red lines) yields more accurate TC forecasts compared with the GSI default cloud detection (blue and dark blue lines), and the assimilation of ATMS (solid lines) provides better forecasts than the assimilation of AMSU-A (dashed lines).

From late 26 October to 28 October, Hurricane Sandy moved northeast parallel to the eastern coastline of the United States. However, it took a hard left turn toward the west, and struck the coast perpendicularly, late on 29 October. To verify that the forecasts successfully capture the sharp turn, the 72-h hurricane tracks at 1200 and 1800 UTC 26 October are compared with the best track in Figs. 8a and 8b, respectively. The tracks of the ATMS_VIIRS most closely approach the NHC best track for both 1200 and 1800 UTC while the AMSUA_GSI tracks are far from the turning point. To access the diagnostic information from the forecasted atmospheric status, Figs. 9a and 9c display the difference in geopotential height (shaded) between AMSUA_GSI and ATMS_GSI, and geopotential height (contour) at the 72-h forecast from 1800 UTC 26 October for AMSUA_MOD and ATMS_VIIRS, respectively. The difference in geopotential height and temperature in Figs. 9a and 9b shows that the geopotential height and temperature from AMSUA_MOD are lower and warmer than those from AMSUA_GSI in the northwest portion of the hurricane center, respectively, and it is the opposite in southeast portion of the center. The differences indicate that the hurricane center of the AMSUA_MOD is located to the northwest of the AMSUA_GSI. For the ATMS_VIIRS experiment in Figs. 9c and 9d, the region west of the hurricane center has a negative geopotential height difference and positive temperature difference, while east of the center is the reverse. Compared to AMSU-A, the magnitudes of the differences are relatively small. These biases indicate that the hurricane center from ATMS_VIIRS slightly leans to the west compared with that from ATMS_GSI. The hurricane track comparison agrees well with the track RMSE analysis in that forecasts using the subpixel cloud detection and the ATMS measurements produce more accurate forecast results than the GSI cloud detection and AMSU-A measurements.

To assess the impact of the different cloud screenings on the radiance assimilation and the track forecasts, an

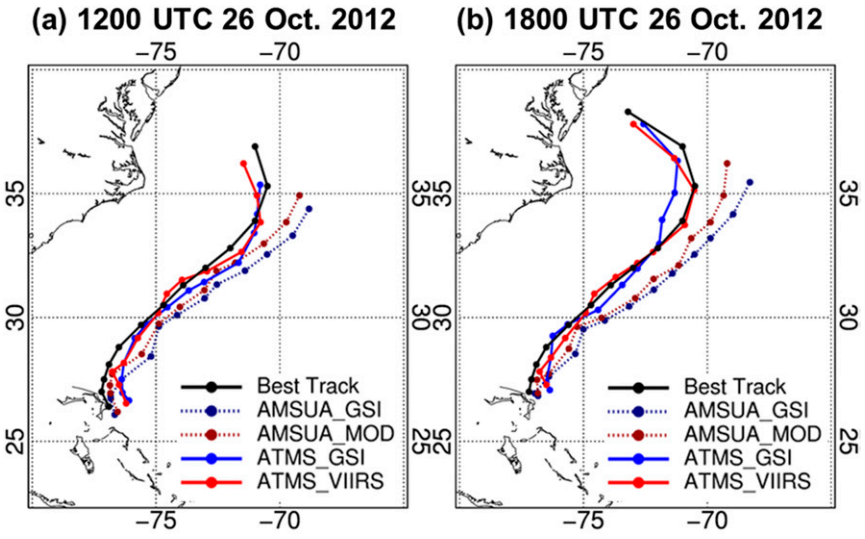

FIG. 8. Hurricane Sandy tracks of the best track and 72-h forecasts from (a) 1200 UTC 26 Oct and (b) 1800 UTC 26 Oct 2012 for AMSUA_MOD (dark red dotted line), AMSUA_GSI (dark blue dotted line), ATMS_VIIRS (red solid line), and ATMS_GSI (blue solid line).

attempt is made to analyze the thermodynamic and synoptic-scale status. Since the assimilation impact for the AMSU-A experiments is more obvious than for the ATMS experiments for the forecast from 1800 UTC 26 October, the analysis and forecast fields of the AMSUA_MOD and AMSUA_GSI are compared for this forecast time.

To extract the difference in the assimilation effect between AMSUA_MOD and AMSUA_GSI at 1800 UTC 26 October, temperature increments of the analysis fields (A) from the background field (B) at 300 hPa (T_{A-B}) are calculated. The deviation of AMSUA_GSI T_{A-B} from AMSUA_MOD T_{A-B} (AMSUA_MOD T_{A-B} minus AMSUA_GSI T_{A-B}; DT_{A-B}) is displayed in Fig. 10a. It shows a comparison of the assimilation's effect of the subpixel cloud-detection method on the temperature field with that of the GSI default QC scheme. Significantly positive and negative DT_{A-B} are shown in the northeast and west of the hurricane center, respectively. The assimilation impact on the temperature field is directly reflected in the geopotential height. Figure 10b displays the geopotential height differences (shaded) at 300 hPa between the AMSUA_MOD and AMSUA_GSI analysis fields along with the analysis field of geopotential heights (solid and dotted lines). A strong ridge is located east of the hurricane, and the use of the subpixel cloud-detection method strengthens the ridge as shown in Fig. 10a as the positive DT_{A-B}. Over the western part of the hurricane, the geopotential height from AMSUA_MOD is slightly lower than that from AMSUA_GSI. Figure 10c displays the geopotential height of the 60-h forecast valid at 0600 UTC 29 October when the hurricane turned toward the northwest. During the forecast, the northwest trough deepened due to the strong blocking ridge of the analysis field shown in Fig. 10b. Comparing the forecasted geopotential heights from the AMSUA_MOD and AMSUA_GSI, the trough and ridge from the AMSUA_MOD are stronger than those from the AMSUA_GSI. The wind speed and direction at 500 hPa are also compared in Fig. 10d. The shaded areas and arrows indicate the differences in wind speed and wind direction, respectively. In eastern New Jersey, where Sandy made landfall, the wind speed difference is positive and the arrows point northwest. These wind speed and direction differences indicate that the AMSUA_MOD shows a northwest wind toward the northeast coast of the United States, and the wind speed is higher than that from AMSUA_GSI. The stronger blocking ridge, deeper trough, and higher wind speed toward the northeast coast from the AMSUA_MOD are derived from a different cloud screening method. The thermodynamic and synoptic-scale status from the AMSUA_MOD result in the northwestward movement of Sandy, which is closer to the best track than that from the AMSUA_GSI.

b. Typhoon Haiyan

The errors of the Typhoon Haiyan track, SLP, and MWS forecasts are calculated against the Regional Specialized Meteorological Center (RSMC) Tokyo-Typhoon Center best track dataset. The track RMSEs for various CF thresholds are given in Figs. 11a and 11b. As with the track errors from the Sandy forecast in Fig. 3, the track RMSE has its minimum when a CF threshold balances

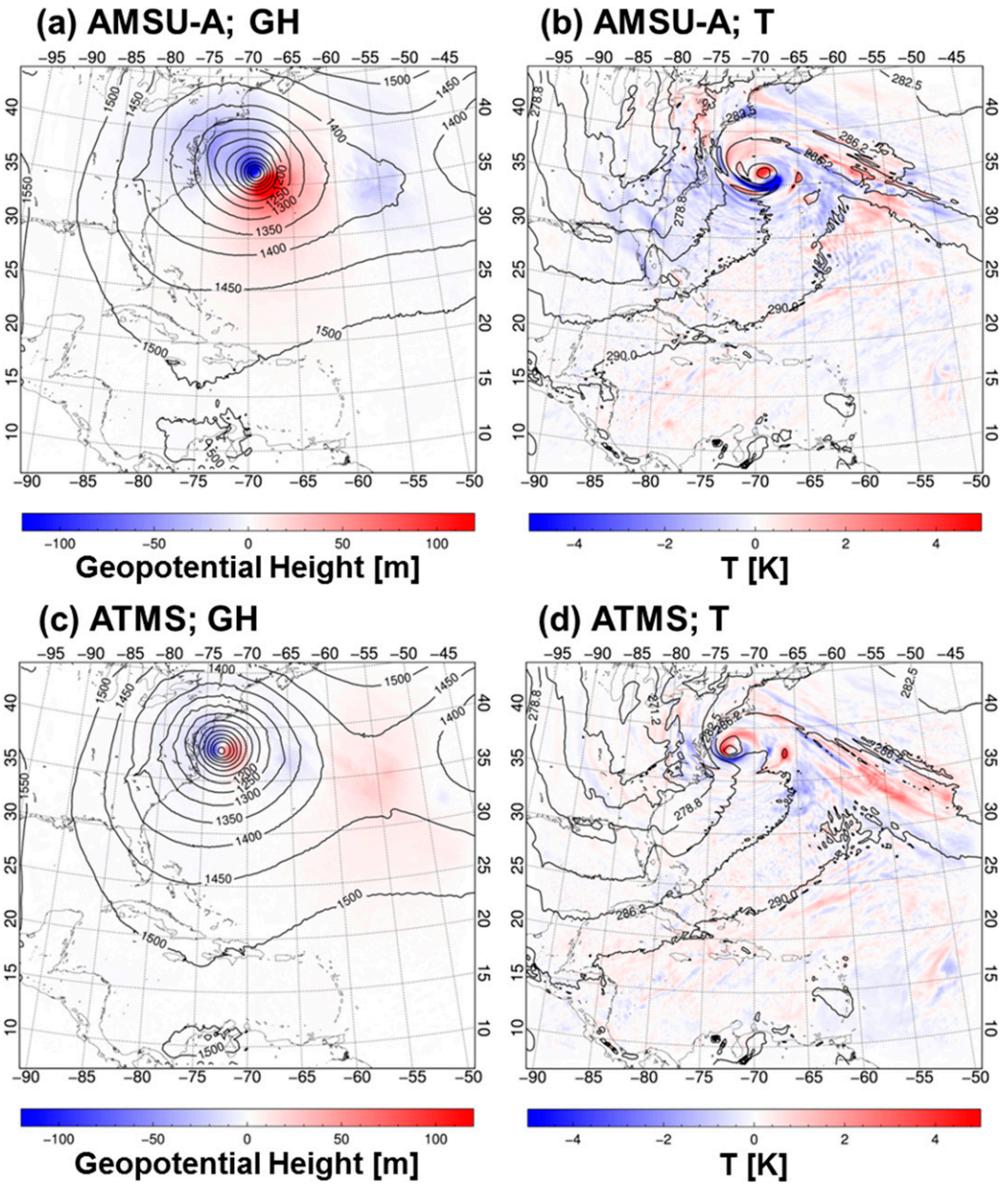

FIG. 9. (a),(c) The geopotential height and (b),(d) temperature at 850 hPa for (a),(b) AMSUA_MOD and (c),(d) ATMS_VIIRS at the 72-h forecast from 1800 UTC 26 Oct 2012 (valid time: 1800 UTC 29 Oct) are plotted as contours. The difference in (a),(c) geopotential height and (b),(d) temperature from AMSU-A experiments [(a),(b) (AMSUA_MOD − AMSUA_GSI)] and ATMS experiments [(c),(d) ATMS_VIIRS − ATMS_GSI] are color shaded.

the data usage and the reduction in cloud contamination. The AMSU-A experiment has the smallest track RMSE of 172.1 km with CF thresholds of about 10% and 20%, while CF thresholds of around 80% and 90% minimize the ATMS track RMSEs. The RMSEs of the AMSU-A experiments for the 72-h forecast time at CF thresholds of 10% and 20% are 173.2 and 172.1 km, respectively, while the ATMS experiments have RMSEs of 151.7 and 125.1 km at CF thresholds of 80% and 90%, respectively. This is similar to the track error analysis for the Sandy experiment. Without the humidity-sounding channels, ATMS radiances from the 12 temperature-sounding channels are assimilated, and the track errors are shown in Fig. 11c. Similar to the ATMS_T experiment for Sandy, the track error rapidly decreases with an increasing CF up to 20%. A CF threshold for the

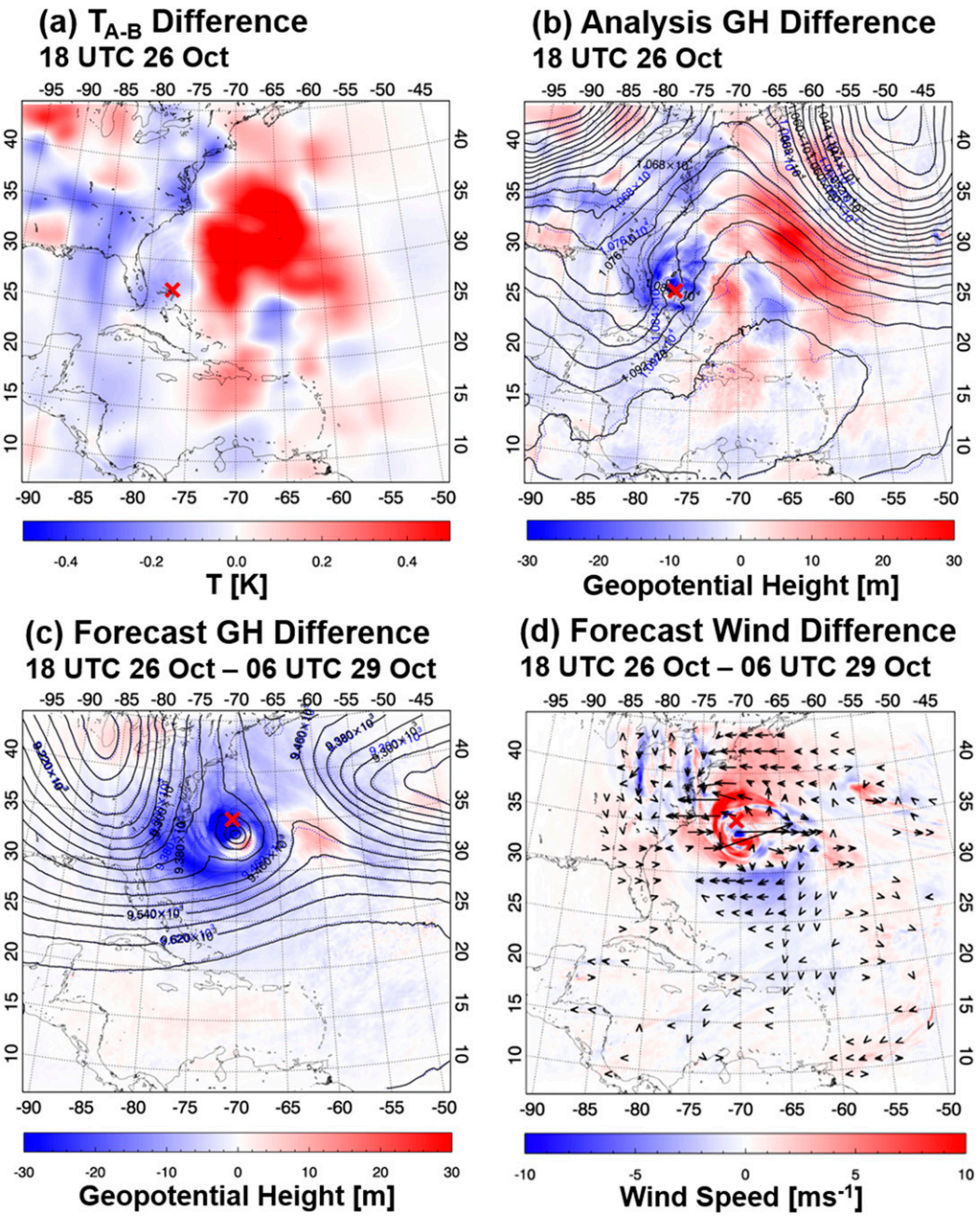

FIG. 10. The difference (AMSUA_MOD − AMSUA_GSI) in (a) 300 hPa T_{A-B} at 1800 UTC 26 Oct, (b) the 300-hPa analysis field geopotential height at 1800 UTC 26 Oct, (c) the 60-h forecast geopotential height at 300 hPa from 1800 UTC 26 Oct (valid time: 0600 UTC 29 Oct), and (d) 60-h forecasted wind speed at 500 hPa from 1800 UTC 26 Oct are color shaded. The black solid and blue dotted lines in (c),(d) indicate AMSUA_MOD and AMSUA_GSI geopotential heights, respectively. Arrows in (d) shows the difference in the direction of the wind between AMSUA_MOD and AMSUA_GSI (AMSUA_MOD − AMSUA_GSI). The × signs indicate the center of Hurricane Sandy.

minimum track errors is not clear, but it seems to be about 50%. As noted earlier, AMSU-A measurements need more strict CF thresholds to remove the cloud-contaminated radiances due to the absence of the strong H_2O absorption band. Contrary to the track RMSE, the correlation between the intensity RMSEs and the CF threshold is less clear, and it is hard to find a definitive CF threshold to minimize the intensity RMSE (not shown).

Considering the track errors of the Haiyan forecast, CF thresholds of 10% for the AMSU-A/MODIS cloud

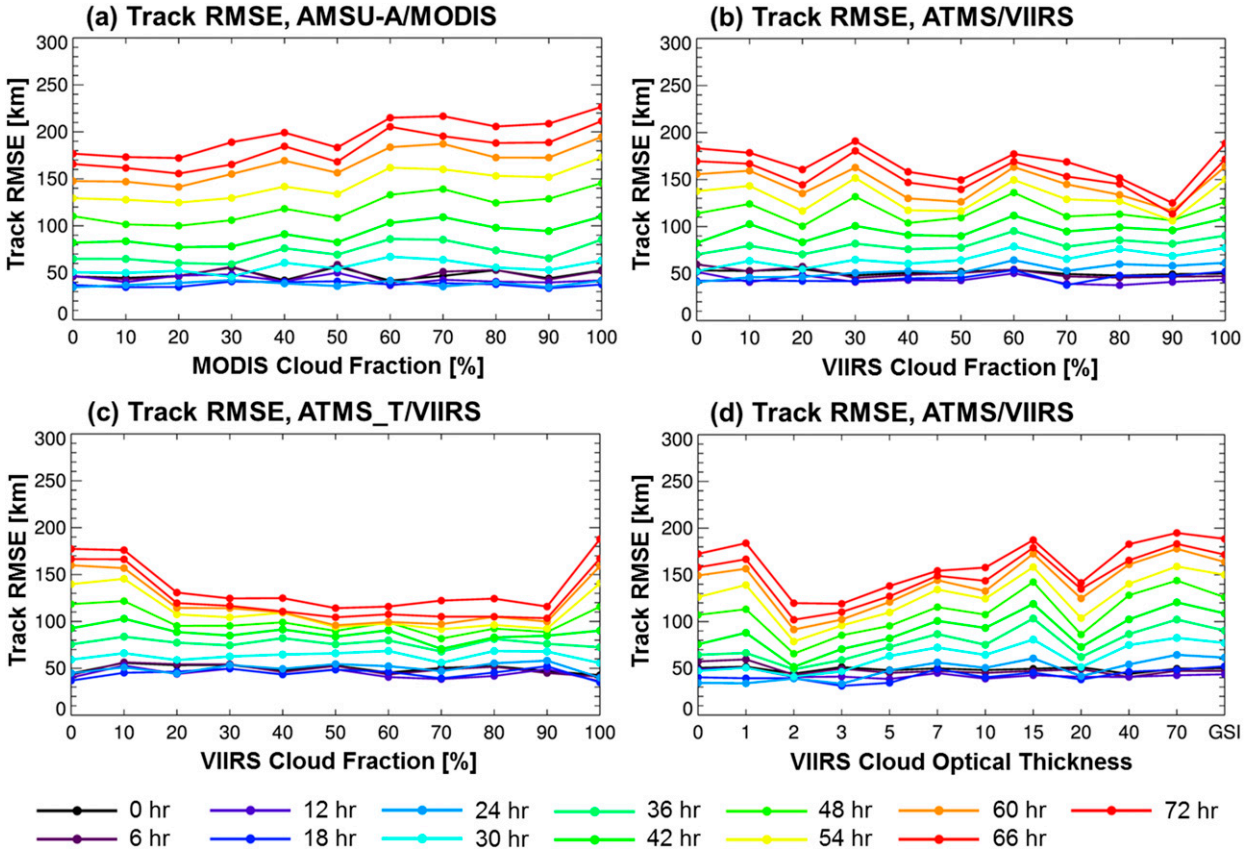

FIG. 11. The track RMSEs for various CF thresholds of Typhoon Haiyan experiments for (a) AMSU-A/MODIS, (b) ATMS/VIIRS, and (c) ATMS_T/VIIRS. The track RMSEs for various COT thresholds for (d) ATMS/VIIRS with the different colors showing the different forecast times.

detection (hereafter AMSUA_MOD10) are selected. Their track, SLP, and MWS RMSEs and mean biases are displayed in Fig. 12. For comparison, track errors from the experiments using the GSI cloud detection (AMSUA_GSI) and the AMSU-A/MODIS cloud detection with a CF threshold of 90% (hereafter AMSUA_MOD90) are also plotted. The error differences between AMSUA_MOD10 and AMSUA_GSI are close to zero before the 18-h forecast time. However, the difference increased with forecast time by 53.4 km in RMSE and 46.0 km in mean bias at the 72-h forecast time, showing a noteworthy improvement through use of the MODIS cloud product. The AMSUA_MOD90 also reduces the track error of the Haiyan forecasts, although the effect of the subpixel cloud detection is less significant than that of the AMSUA_MOD10. For the SLP RMSE, the comparable results are shown in the three experiments, all three show very similar results, unlike for the track error analysis. MWS RMSEs of the AMSUA_MOD10 and AMSUA_MOD90 show improvements before the 30-h forecast: $\sim$1.4 m s^{-1} for AMSUA_MOD10 and $\sim$2.2 m s^{-1} for AMSUA_MOD90. SLP and MWS absolute mean biases from the AMSUA_MOD10 are slightly smaller than other mean biases, but the confidence intervals are obviously larger than the mean bias differences. Comparing the confidence intervals, the improvement in SLP and MWS mean biases is almost negligible for the Haiyan experiments. Given the large forecast RMSEs and confidence intervals, it is apparent that the intensity forecast for Haiyan falls behind that for Sandy. Studies have investigated the difficulty in predicting TC intensity due to the limitation of NWP modeling (DeMaria et al. 2014; WMO 2015). It makes little improvement in the accuracy of the intensity forecasts while the track forecasts have been steadily enhanced (DeMaria et al. 2014). Also, uncertainty of the SLP and MWS observations partly contributes to the relatively large bias and RMSE of the intensity forecasts. For this case, the impact of the subpixel cloud-detection method is not as clear as for the Sandy experiments due to the large uncertainties in the intensity forecasts.

Based on the error analysis for various CF thresholds, CF $<$ 80% for the ATMS experiments (hereafter ATMS_VIIRS) was determined as the optimal threshold.

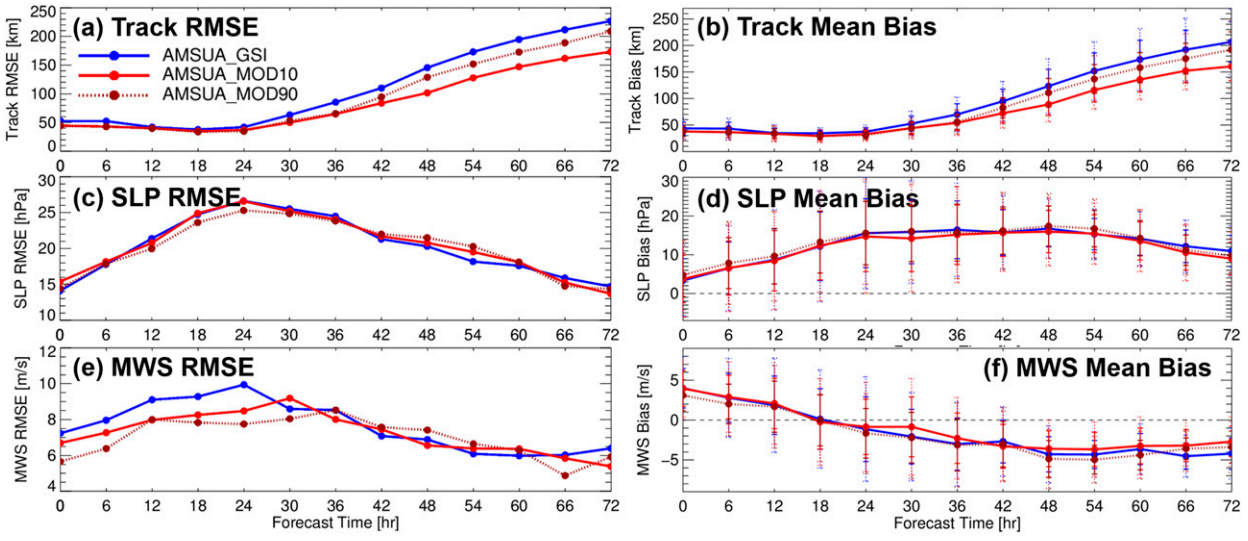

FIG. 12. (a),(b) The track; (c),(d) SLP; and (e),(f) MWS (a),(c),(e) RMSEs and (b),(d),(f) mean biases of Typhoon Haiyan experiments for AMSUA_GSI (blue solid line), AMSUA_MOD10 (red solid line), and AMSUA_MOD90 (dark red dotted line). Solid and dotted vertical bars indicate the 80% and 95% confidence intervals of the mean biases, respectively.

Figure 13 shows the track, SLP, and MWS RMSEs and mean biases from ATMS_GSI and ATMS_VIIRS. The track error difference between the ATMS_VIIRS and ATMS_GSI shows a pattern that is similar to the comparison of AMSUA_MOD10 and AMSUA_GSI. The RMSEs and mean biases from the ATMS_VIIRS are obviously smaller than those from the ATMS_GSI with improvements of 36.8 km in RMSE and 29.3 km in mean bias at the 72-h forecast, indicating an overall reduction in track forecast error. The improvement from using high spatial resolution cloud products becomes more significant after the 36-h forecast. The SLP RMSE is reduced before the 24-h forecast when the subpixel cloud-detection method is applied with a maximum improvement of 6.0 hPa. For MWS RMSE, the ATMS_GSI and ATMS_VIIRS have comparable results. The mean biases of SLP and MWS from the ATMS_VIIRS are slightly reduced, and their uncertainties are smaller than those from the AMSU-A experiments.

The track errors from the experiments using AMSU-A and ATMS are compared (plotted in separate figures). Prior to the 42-h forecast, the ATMS_GSI track

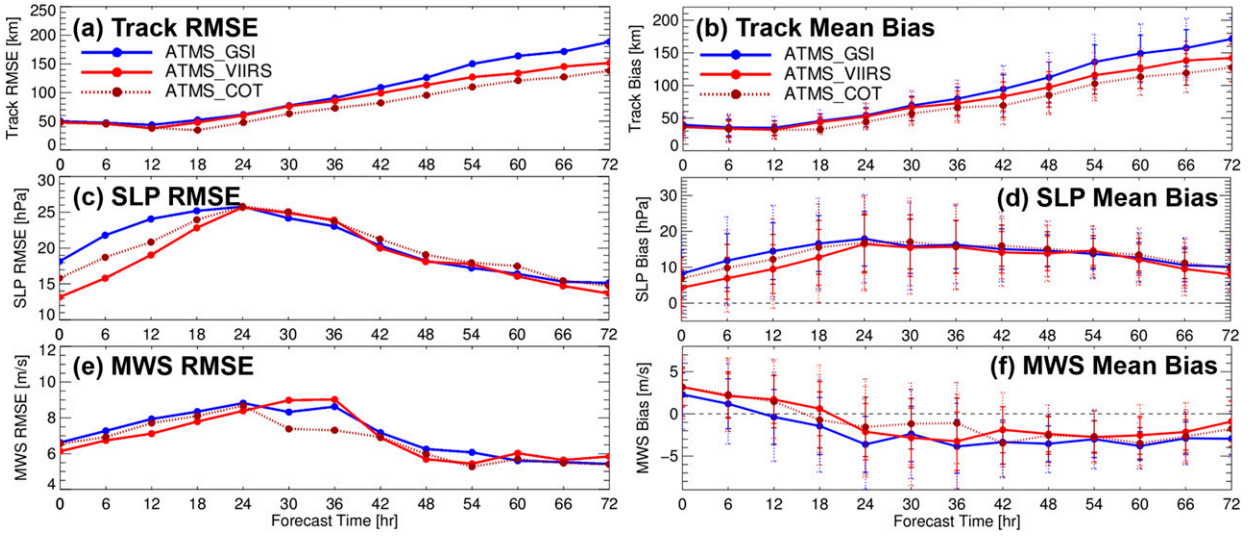

FIG. 13. (a),(b) The track; (c),(d) SLP, and (e),(f) MWS (a),(c),(e) RMSEs and (b),(d),(f) mean biases of Typhoon Haiyan experiments for ATMS_GSI (blue solid line), ATMS_VIIRS (red solid line), and ATMS_COT (red dotted line). Solid and dotted vertical bars in the right column indicate the 80% and 95% confidence intervals of the mean biases, respectively.

RMSEs are comparable or slightly larger than the errors from the AMSUA_GSI. However, the AMSUA_GSI errors overtake those from the ATMS_GSI after 42 h, and the difference in track RMSE increased by 43.5 km at the 72-h forecast. Similarly, the track mean bias from the ATMS_VIIRS at the 72 h forecast is 142.1 km, while that from AMSUA_MOD10 is 160.5 km. For the SLP and MWS forecast, ATMS_VIIRS is comparable to AMSUA_MOD10 or gives a smaller error. This forecast error reduction in the ATMS experiment indicates that the use of the ATMS measurements produces better performance than the use of the AMSU-A radiances. Potential reasons for the improvements could be the differences in the channels used, the data quality between the AMSU-A and ATMS measurements such as spatial resolution, and the slight deteriorating performance of AMSU-A/*Aqua*.

Since microwave radiances are affected by precipitation particles, a nonprecipitating cloud is relatively transparent at microwave wavelengths unlike an ice and/or precipitating cloud. Cloud products from the imager sensors, however, basically cannot distinguish sharply between precipitating and nonprecipitating clouds because the products are based on IR and VIS measurements. Therefore, the subpixel cloud-detection method finds the cloud-affected microwave radiances indirectly, without knowledge of the presence of precipitating clouds. Cloud water amount and COT are directly related to the cloud signal in the microwave wavelengths, because a possibility of precipitation highly depends on the quantitative amount of cloud water. In this study, the CF is used instead of the cloud water path or COT due to the limited MODIS and VIIRS cloud products. Since only daytime MODIS water path and COT are available, the visible-based products are excluded to avoid an inconsistent application of the cloud detection on day and night assimilations. Experiments using MODIS water path and COT provide unclear and incoherent results (not shown in this paper). VIIRS yields COT for both day and night, but products before 27 April 2013 are not available to the public. Although the VIIRS COT retrieval algorithms for day and night are not identical, use of day and night VIIRS COT could minimize the inconsistency in the subpixel cloud detection of the experiment using MODIS water path and COT.

A similar approach to obtain the ATMS CF is applied to collocated ATMS and VIIRS COT for Typhoon Haiyan. All available VIIRS COTs within a given ATMS FOV are averaged and collocated with the ATMS microwave radiance. The ATMS radiances are then assimilated into the system for various VIIRS COT thresholds. The track errors of these forecasts are given in Fig. 11d. The RMSEs show that the subpixel cloud detection using COT thresholds, COT $<$ 2–10, can improve the track forecast. We selected a COT threshold, COT $<$ 5, and the results of the experiment (ATMS_COT) are plotted in Fig. 13 with dotted lines. For the track forecast, the ATMS_COT has a smaller RMSE and mean bias than those of the ATMS_GSI and ATMS_VIIRS. The improvement in intensity forecast is generally comparable with that of the experiment using the VIIRS CF. The comparison between the ATMS_VIIRS and ATMS_COT forecasts in Fig. 13 shows the potential of COT in the subpixel cloud-detection method for TC data assimilation.

Numerous agencies produce best-track data using different analysis methods. Each agency may have intensities that largely deviate from each other (Knapp and Kruk 2010). The track and intensity from RSMC are compared with that from JTWR for Typhoon Haiyan. Tracks are almost identical, but differences are shown in intensity. SLP and MWS of JTWR are generally higher than that of RSMC. Mean biases and RMSEs of the WRF forecasts are calculated against the JTWC best-track data (not shown here). The errors of the experiments using the subpixel cloud-detection method are comparable or slightly smaller than that from the experiments using the GSI default algorithm, showing that the comparison against JTWC best-track data is similar with that using RSMC.

6. Summary

A methodology for microwave subpixel cloud detection with collocated high spatial resolution cloud products has been developed, and its impact on radiance assimilation for Hurricane Sandy (2012) and Typhoon Haiyan (2013) has been studied with WRF/GSI. It has been shown that the MODIS and VIIRS CM products can be used for AMSU-A and ATMS subpixel cloud characterization for radiance assimilation, respectively. After cloud detection with MODIS or VIIRS, microwave radiance assimilation improves the Hurricane Sandy (2012) forecasts by 0–38.0 km for the track and 0–3 hPa for SLP. The subpixel cloud detection also reduces the track error (RMSE) of the Typhoon Haiyan (2013) forecast, up to 63 km. The track error analysis shows a difference in the CF thresholds that minimizes the track error between the AMSU-A and ATMS experiments; the AMSU-A experiments have the smallest errors with CF thresholds of 20%–40%, while the ATMS experiments have the smallest errors with CF thresholds of 60%–90%. This discrepancy results from the spectral channel difference between these two microwave instruments. Since the signal of the water vapor continuum around 50.3–58.3 GHz is relatively small, more

strict cloud screening thresholds are required (lower CF numbers) to obtain information about the water vapor profile and minimize the impact of clouds without the strong absorption by water vapor at 183 GHz. There are, of course, other possible reasons for the CF threshold differences. First, the spatial resolution is different between the microwave sensors. Relatively coarse spatial resolution AMSU-A measurements are more easily contaminated by clouds, thereby requiring lower CF numbers than ATMS to remove these cloud effects. The performance of the GSI default cloud-detection algorithm for AMSU-A and ATMS, and the accuracy of the MODIS and VIIRS CM products could also explain the CF threshold discrepancy. The CF threshold for microwave subpixel cloud detection can be decided by the characteristics of the sensors and their collocated cloud products.

Considering the results of the Hurricane Sandy and Typhoon Haiyan experiments, CF thresholds between 50% and 90% generally improve the track forecast for both the AMSU-A and ATMS experiments. The use of collocated VIIRS COT for Typhoon Haiyan shows the usefulness of COT in the subpixel cloud-detection method for TC data assimilation. Moreover, it shows a potential of other cloud products, such as cloud phase and cloud-top pressure. This method has been applied to recent TC cases including not only large systems such as Sandy and Haiyan but also a relatively small TC, namely Tropical Storm Linfa (2015). Preliminary results, not shown in this paper, indicate that use of subpixel cloud detection has a positive impact on this relatively small TC, as well as large systems.

Another noticeable improvement is in the use of ATMS. In general, forecasts using the ATMS measurements outperform those using AMSU-A. Although it is hard to pinpoint one specific reason from this study, data quality and the use of more channels in the ATMS data could contribute to these improvements. The slight deteriorating performance of AMSU-A/*Aqua* might be another reason.

Since a spatial resolution and weighting function peak for a given channel are decided by its spectral frequency, whether an observed radiance is cloud contaminated or not varies depending on the spectral channels. From this, it might be deduced that a separate application of the cloud-detection method to each channel yields more accurate cloud screening and data assimilation. In this study, however, the subpixel cloud detection is performed regardless of the resolution and weighting function difference. Further research should be directed to elaborate the algorithm by considering this issue.

Comparing atmospheric profiles of the analysis fields and radiosondes shows improvement in moisture fields below 500 hPa in Fig. 4. From above, it is highly probable that the subpixel cloud-detection method used here has the potential to enhance the forecast of other atmospheric phenomena beyond TCs, and can be applied to a global NWP model. This method can also be applied to process measurements from other pairs of microwave sounder and imager cloud products. AMSU-A and MHS/Advanced Very High Resolution Radiometer (AVHRR) on board the European Organization for the Exploitation of Meteorological Satellites (EUMETSAT) *Metop-A/-B*, and the Microwave Atmospheric Temperature Sounder (MWTS) and Microwave Atmospheric Humidity Sounder (MWHS)/Medium Resolution Spectral Imager (MERSI) on board the Chinese *FY-3* series (Dong et al. 2009) may also be used for improved data assimilation, especially for improved near-real-time (NRT) assimilation of microwave sounder radiances from direct broadcast (DB) sites.

Acknowledgments. This work is partly supported by the JPSS visiting scientist and GOES-R high impact weather programs under Grant NA10NES4400013. The views, opinions, and findings contained in this report are those of the authors and should not be construed as an official National Oceanic and Atmospheric Administration or U.S. government position, policy, or decision. B.-J. Sohn was supported by the Korea Meteorological Administration Research and Development Program under Grant KMIPA 2015-1060. Juan Li was supported by CMA GYHY20140611. The authors also acknowledge the CISL Research Data Archive (http://rda.ucar.edu/), GES DISC (http://disc.sci.gsfc.nasa.gov/), LAADS Web (https://ladsweb.nascom.nasa.gov/), and NOAA CLASS (http://www.class.ngdc.noaa.gov/) websites for the online use of their valuable data.

REFERENCES

Ackerman, S. A., K. I. Strabala, W. P. Menzel, R. A. Frey, C. C. Moeller, and L. E. Gumley, 1998: Discriminating clear sky from clouds with MODIS. *J. Geophys. Res.*, **103**, 32 141–32 157, doi:10.1029/1998JD200032.

——, R. A. Frey, K. I. Strabala, Y. Liu, L. E. Gumley, B. Baum, and W. P. Menzel, 2010: Discriminating clear-sky from cloud with MODIS algorithm theoretical basis document (MOD35) version 6.1. Doc. ATBD-MOD-06, 117 pp. [Available online at http://modis.gsfc.nasa.gov/data/atbd/atbd_mod06.pdf.]

Baker, N., 2012: Joint Polar Satellite System (JPSS) cloud top algorithm theoretical basis document (ATBD). Joint Polar Satellite System (JPSS) Ground Project, Code 474, Doc. 474-00041, 73 pp. [Available online at http://npp.gsfc.nasa.gov/sciencedocs/2015-06/474-00041_ATBD-Cloud-Top_A.pdf.]

Bauer, P., A. J. Geer, P. Lopez, and D. Salmond, 2010: Direct 4D-Var assimilation of all-sky radiances. Part I: Implementation. *Quart. J. Roy. Meteor. Soc.*, **136**, 1868–1885, doi:10.1002/qj.659.

——, G. Ohring, C. Kummerow, and T. Auligne, 2011: Assimilating satellite observations of clouds and precipitation into NWP models. *Bull. Amer. Meteor. Soc.*, **92**, ES25–ES28, doi:10.1175/2011BAMS3182.1.

Baum, B. A., W. P. Menzel, R. A. Frey, D. C. Tobin, R. E. Holz, S. A. Ackerman, A. K. Heidinger, and P. Yang, 2012: MODIS cloud-top property refinements for Collection 6. *J. Appl. Meteor. Climatol.*, **51**, 1145–1163, doi:10.1175/JAMC-D-11-0203.1.

Blake, E. S., T. B. Kimberlain, R. J. Berg, J. P. Cangialosi, and J. L. Beven II, 2013: Tropical Cyclone Report: Hurricane Sandy 22–29 October 2012. Tropical Cyclone Rep. AL182012, 157 pp. [Available online at http://www.nhc.noaa.gov/data/tcr/AL182012_Sandy.pdf.]

Bormann, N., A. Fouilloux, and W. Bell, 2013: Evaluation and assimilation of ATMS data in the ECMWF system. *J. Geophys. Res. Atmos.*, **118**, 12 970–12 980, doi:10.1002/2013JD020325.

Chen, Y., F. Weng, Y. Han, and Q. Liu, 2008: Validation of the Community Radiative Transfer Model by using CloudSat data. *J. Geophys. Res.*, **113**, D00A03, doi:10.1029/2007JD009561.

DeMaria, M., C. R. Sampson, J. A. Knaff, and K. D. Musgrave, 2014: Is tropical cyclone intensity guidance improving? *Bull. Amer. Meteor. Soc.*, **95**, 387–398, doi:10.1175/BAMS-D-12-00240.1.

Diak, G. R., D. Kim, M. S. Whipple, and X. Wu, 1992: Preparing for the AMSU. *Bull. Amer. Meteor. Soc.*, **73**, 1971–1984, doi:10.1175/1520-0477(1992)073<1971:PFTA>2.0.CO;2.

Dong, C., and Coauthors, 2009: An overview of a new Chinese weather satellite FY-3A. *Bull. Amer. Meteor. Soc.*, **90**, 1531–1544, doi:10.1175/2009BAMS2798.1.

English, S., 2014: Satellite data assimilation at NCEP. *2014 JCSDA Seminars*, College Park, MD, Joint Center for Satellite Data Assimilation. [Available online at http://www.jcsda.noaa.gov/documents/seminardocs/2014/English20141020.pptx.]

Geer, A. J., P. Bauer, and P. Lopez, 2010: Direct 4D-Var assimilation of all-sky radiances. Part II: Assessment. *Quart. J. Roy. Meteor. Soc.*, **136**, 1886–1905, doi:10.1002/qj.681.

Godin, R., 2014a: Joint Polar Satellite System (JPSS) VIIRS cloud mask (VCM) algorithm theoretical basis document (ATBD). Joint Polar Satellite System (JPSS) Ground Project, Code 474, Doc. 474-00033, 101 pp. [Available online at http://npp.gsfc.nasa.gov/sciencedocs/2015-06/474-00033_ATBD-VIIRS-Cloud-Mask_E.pdf.]

——, 2014b: Joint Polar Satellite System (JPSS) cloud effective particle size and cloud optical thickness algorithm theoretical basis document (ATBD). Joint Polar Satellite System (JPSS) Ground Project, Code 474, Doc. 474-00042, 148 pp. [Available online at http://npp.gsfc.nasa.gov/sciencedocs/2015-06/474-00042_ATBD-VIIRS-Cloud-EPS-COT_A.pdf.]

Goerss, J. S., 2009: Impact of satellite observations on the tropical cyclone track forecasts of the Navy Operational Global Atmospheric Prediction System. *Mon. Wea. Rev.*, **137**, 41–50, doi:10.1175/2008MWR2601.1.

Han, Y., P. van Delst, Q. Liu, F. Weng, B. Yan, R. Treadon, and J. Derber, 2006: JCSDA Community Radiative Transfer Model (CRTM), version 1. NOAA Tech. Rep. NESDIS-122, 33 pp.

Hewison, T. J., and S. J. English, 1999: Airborne retrievals of snow and ice surface emissivity at millimeter wavelengths. *IEEE Trans. Geosci. Remote Sens.*, **37**, 1871–1879, doi:10.1109/36.774700.

Hong, S.-Y., and J.-O. J. Lim, 2006: The WRF single-moment 6-class microphysics scheme (WSM6). *J. Korean Meteor. Soc.*, **42**, 129–151.

——, Y. Noh, and J. Dudhia, 2006: A new vertical diffusion package with an explicit treatment of entrainment processes. *Mon. Wea. Rev.*, **134**, 2318–2341, doi:10.1175/MWR3199.1.

Hu, M., and M. Xue, 2007: Implementation and evaluation of cloud analysis with WSR-88D reflectivity data for GSI and WRF-ARW. *Geophys. Res. Lett.*, **34**, L07808, doi:10.1029/2006GL028906.

——, H. Shao, D. Stark, K. Newman, and C. Zhou, Eds., 2014: Gridpoint Statistical Interpolation (GSI) community version 3.3 user's guide. NOAA Developmental Testbed Center, 108 pp. [Available at http://www.dtcenter.org/com-GSI/users/docs/users_guide/GSIUserGuide_v3.3.pdf.]

Hutchison, K. D., J. K. Roskovensky, J. M. Jackson, A. K. Heidinger, T. J. Kopp, M. J. Pavolonis, and R. Frey, 2005: Automated cloud detection and classification of data collected by the Visible Infrared Imager Radiometer Suite (VIIRS). *Int. J. Remote Sens.*, **26**, 4681–4706, doi:10.1080/01431160500196786.

Joint Typhoon Warning Center, 2013: Annual tropical cyclone report 2013. Tech. Doc., JTWC, 143 pp. [Available online at http://www.usno.navy.mil/NOOC/nmfc-ph/RSS/jtwc/atcr/2013atcr.pdf.]

Joo, S., J. Eyre, and R. Marriott, 2013: The impact of MetOp and other satellite data within the Met Office global NWP system using an adjoint-based sensitivity method. *Mon. Wea. Rev.*, **141**, 3331–3342, doi:10.1175/MWR-D-12-00232.1.

Kain, J. S., 2004: The Kain–Fritsch convective parameterization: An update. *J. Appl. Meteor.*, **43**, 170–181, doi:10.1175/1520-0450(2004)043<0170:TKCPAU>2.0.CO;2.

King, M. D., and Coauthors, 2003: Cloud and aerosol properties, precipitable water, and profiles of temperature and water vapor from MODIS. *IEEE Trans. Geosci. Remote Sens.*, **41**, 442–458, doi:10.1109/TGRS.2002.808226.

Kleist, D. T., D. F. Parrish, J. C. Derber, R. Treadon, W.-S. Wu, and S. Lord, 2009: Introduction of the GSI into the NCEP global data assimilation system. *Wea. Forecasting*, **24**, 1691–1705, doi:10.1175/2009WAF2222201.1.

Knapp, K., and M. C. Kruk, 2010: Quantifying interagency differences in tropical cyclone best-track wind speed estimates. *Mon. Wea. Rev.*, **138**, 1459–1476, doi:10.1175/2009MWR3123.1.

Lander, M., C. Guard, and S. J. Camargo, 2014: Super-Typhoon Haiyan [in "State of the Climate in 2013"]. *Bull. Amer. Meteor. Soc.*, **95** (7), S112–S114.

Lee, T. F., S. D. Miller, F. J. Turk, C. Schueler, R. Julian, S. Deyo, P. Dills, and S. Wang, 2006: The NPOESS VIIRS day/night visible sensor. *Bull. Amer. Meteor. Soc.*, **87**, 191–199, doi:10.1175/BAMS-87-2-191.

Li, J., and X. Zou, 2013: A quality control procedure for FY-3A MWTS measurements with emphasis on cloud detection using VIRR cloud fraction. *J. Atmos. Oceanic Technol.*, **30**, 1704–1715, doi:10.1175/JTECH-D-12-00164.1.

——, W. P. Menzel, Z. Yang, R. A. Frey, and S. A. Ackerman, 2003: High-spatial-resolution surface and cloud-type classification from MODIS multi-spectral band measurements. *J. Appl. Meteor.*, **42**, 204–226, doi:10.1175/1520-0450(2003)042<0204:HSRSAC>2.0.CO;2.

——, ——, F. Sun, T. J. Schmit, and J. Gurka, 2004: AIRS subpixel cloud characterization using MODIS cloud products. *J. Appl. Meteor.*, **43**, 1083–1094, doi:10.1175/1520-0450(2004)043<1083:ASCCUM>2.0.CO;2.

Li, Z., J. Li, T. J. Schmit, W. P. Menzel, and S. A. Ackerman, 2007: Comparison between current and future environmental satellite imagers on cloud classification using MODIS. *Remote Sens. Environ.*, **108**, 311–326, doi:10.1016/j.rse.2006.11.023.

Liu, Z., C. S. Schwartz, C. Snyder, and S.-Y. Ha, 2012: Impact of assimilating AMSU-A radiances on forecasts of 2008 Atlantic

tropical cyclones initialized with a limited-area ensemble Kalman filter. *Mon. Wea. Rev.*, **140**, 4017–4034, doi:10.1175/MWR-D-12-00083.1.

McNally, A. P., J. C. Derber, W. Wu, and B. B. Katz, 2000: The use of TOVS level-1b radiances in the NCEP SSI analysis system. *Quart. J. Roy. Meteor. Soc.*, **126**, 689–724, doi:10.1002/qj.49712656315.

Muth, C., W. A. Webb, W. Atwood, and P. Lee, 2005: Advanced technology microwave sounder on the National Polar-orbiting Operational Environmental Satellite System. *Proc. IEEE Int. Conf. on Geoscience and Remote Sensing Symp. 2005*, Seoul, South Korea, Institute of Electrical and Electronics Engineers, 99–102, doi:10.1109/IGARSS.2005.1526113.

Nagle, F. W., 1998: The association of disparate satellite observations. *Proc. Second Symp. on Integrated Observing Systems*, Phoenix, AZ, Amer. Meteor. Soc., 49–52.

——, and R. E. Holz, 2009: Computationally efficient methods of collocating satellite, aircraft, and ground observations. *J. Atmos. Oceanic Technol.*, **26**, 1585–1595, doi:10.1175/2008JTECHA1189.1.

Nakajima, T., and M. D. King, 1990: Determination of the optical thickness and effective particle radius of clouds from reflected solar radiation measurements. Part I: Theory. *J. Atmos. Sci.*, **47**, 1878–1893, doi:10.1175/1520-0469(1990)047<1878:DOTOTA>2.0.CO;2.

National Disaster Risk Reduction and Management Council, 2014: Effects of Typhoon "Yolanda" (Haiyan). SitRep. 108, 62 pp. [Available online at http://www.ndrrmc.gov.ph/attachments/article/1329/Effects_of_Typhoon_YOLANDA_(HAIYAN)_SitRep_No_108_03APR2014.pdf.]

Olsen, E. T., Ed., 2005: AIRS/AMSU/HSB version 4.0 data release user guide. JPL document, Jet Propulsion Laboratory, 72 pp. [Available online at http://daac.gsfc.nasa.gov/AIRS/documentation/v4_docs/V4_Data_Release_UG.pdf.]

Pavolonis, M. J., and A. K. Heidinger, 2004: Daytime cloud overlap detection from AVHRR and VIIRS. *J. Appl. Meteor.*, **43**, 762–778, doi:10.1175/2099.1.

Platnick, S., M. D. King, S. A. Ackerman, W. P. Menzel, B. A. Baum, J. C. Riedi, and R. A. Frey, 2003: The MODIS cloud products: Algorithms and examples from Terra. *IEEE Trans. Geosci. Remote Sens.*, **41**, 459–473, doi:10.1109/TGRS.2002.808301.

Reed, B., 2013: Joint Polar Satellite System (JPSS) Operational Algorithm Description (OAD) document for VIIRS Cloud Optical Properties (COP) Intermediate Product (IP) software. Joint Polar Satellite System (JPSS) Ground Project, Code 474, Doc. 474-00074, 30 pp. [Available online at http://npp.gsfc.nasa.gov/sciencedocs/2015-06/474-00074_OAD-VIIRS-COP-IP_C.pdf.]

Schwartz, C. S., Z. Liu, Y. Chen, and X.-Y. Huang, 2012: Impact of assimilating microwave radiances with a limited-area ensemble data assimilation system on forecasts of Typhoon Morakot. *Wea. Forecasting*, **27**, 424–437, doi:10.1175/WAF-D-11-00033.1.

Skamarock, W. C., and Coauthors, 2008: A description of the Advanced Research WRF version 3. NCAR Tech. Note NCAR/TN-475+STR, 113 pp., doi:10.5065/D68S4MVH.

Stewart, S., 2014: National hurricane center annual summary: 2012 Atlantic Hurricane season. National Hurricane Center, 11 pp. [Available online at http://www.nhc.noaa.gov/data/tcr/summary_atlc_2012.pdf.]

Strabala, K. I., S. A. Ackerman, and W. P. Menzel, 1994: Cloud properties inferred from 8–12-μm data. *J. Appl. Meteor.*, **33**, 212–229, doi:10.1175/1520-0450(1994)033<0212:CPIFD>2.0.CO;2.

Svendsen, E., and Coauthors, 1983: Norwegian Remote Sensing Experiment: Evaluation of the Nimbus 7 scanning multichannel microwave radiometer for sea ice research. *J. Geophys. Res.*, **88**, 2781–2791, doi:10.1029/JC088iC05p02781.

Tomaso, E. D., and N. Bormann, 2012: Assimilation of ATOVS radiances at ECMWF: Second year EUMETSAT fellowship report. EUMETSAT/ECMWF Fellowship Programme Research Rep. 26, 27 pp. [Available online at http://www.ecmwf.int/en/elibrary/9050-assimilation-atovs-radiances-ecmwf-second-year-eumetsat-fellowship-report.]

Wang, P., J. Li, J. Li, Z. Li, T. J. Schmit, and W. Bai, 2014: Advanced infrared sounder subpixel cloud detection with imagers and its impact on radiance assimilation in NWP. *Geophys. Res. Lett.*, **41**, 1773–1780, doi:10.1002/2013GL059067.

——, and Coauthors, 2015: Assimilation of thermodynamic information from advanced infrared sounders under partially cloudy skies for regional NWP. *J. Geophys. Res. Atmos.*, **120**, 5469–5484, doi:10.1002/2014JD022976.

Weng, F., L. Zhao, R. R. Ferraro, G. Poe, X. Li, and N. C. Grody, 2003: Advanced microwave sounding unit cloud and precipitation algorithms. *Radio Sci.*, **38**, 8068, doi:10.1029/2002RS002679.

WMO, 2015: *Eighth International Workshop on Tropical Cyclones (IWTC-VIII)*. Publ. WMO, Jeju, South Korea, World Meteorological Organization, WWRP2015-1. [Available online at http://www.wmo.int/pages/prog/arep/wwrp/tmr/IWTC8.html.]

Wu, W.-S., R. J. Purser, and D. F. Parrish, 2002: Three-dimensional variational analysis with spatially inhomogeneous covariances. *Mon. Wea. Rev.*, **130**, 2905–2916, doi:10.1175/1520-0493(2002)130<2905:TDVAWS>2.0.CO;2.

Zapotocny, T. H., J. A. Jung, J. F. Le Marshall, and R. E. Treadon, 2008: A two-season impact study of four satellite data types and rawinsonde data in the NCEP global data assimilation system. *Wea. Forecasting*, **23**, 80–100, doi:10.1175/2007WAF2007010.1.

Zhang, M., M. Zupanski, M.-J. Kim, and J. A. Knaff, 2013: Assimilating AMSU-A radiances in the TC core area with NOAA operational HWRF (2011) and a hybrid data assimilation system: Danielle (2010). *Mon. Wea. Rev.*, **141**, 3889–3907, doi:10.1175/MWR-D-12-00340.1.

Zou, X., Z. Qin, and F. Weng, 2013: Improved quantitative precipitation forecasts by MHS radiance data assimilation with a newly added cloud detection algorithm. *Mon. Wea. Rev.*, **141**, 3203–3221, doi:10.1175/MWR-D-13-00009.1.